Optical Properties of Moderately-Absorbing Organic and Mixed Organic/Inorganic Particles at Very High Humidities

Final Technical Report for DoE-ASP Grant No.: DE-FG02-08ER64533

Project Duration: June 2008 – December 2011

Tami C. Bond (Principal Investigator), yark@illinois.edu, 217-244-5277
Mark J. Rood (Co-Investigator), mrood@illinois.edu, 217-333-6963
Benjamin T. Brem, Francisco C. Mena-Gonzalez and Yanju Chen (Graduate Student Researchers)

Department of Civil and Environmental Engineering
University of Illinois
205 N. Mathews Ave.,
Urbana, IL 61801, USA

ABSTRACT

Relative humidity (RH) affects the water content of an aerosol, altering its ability to scatter and absorb light, which is important for aerosol effects on climate and visibility. This project involves *in situ* measurement and modeling of aerosol optical properties including absorption, scattering and extinction at three visible wavelengths (467, 530, 660 nm), for organic carbon (OC) generated by pyrolysis of biomass, ammonium sulfate and sodium chloride, and their mixtures at controlled RH conditions. Novel components of this project include investigation of: (1) Changes in all three of these optical properties at scanned RH conditions; (2) Optical properties at RH values up to 95%, which are usually extrapolated instead of measured; and (3) Examination of aerosols generated by the pyrolysis of wood, which is representative of primary atmospheric organic carbon, and its mixture with inorganic aerosol.

Scattering and extinction values were used to determine light absorption by difference and single scattering albedo values. Extensive instrumentation development and benchmarking with independently measured and modeled values were used to obtain and evaluate these new results. The single scattering albedo value for a dry absorbing polystyrene microsphere benchmark agreed within 0.02 (absolute value) with independently published results at 530 nm. Light absorption by a nigrosin (sample light-absorbing) benchmark increased by a factor of 1.24 +/-0.06 at all wavelengths as RH increased from 38 to 95%. Closure modeling with Mie theory was able to reproduce this increase with the linear volume average (LVA) refractive index mixing rule for this water soluble compound.

Absorption by biomass OC aerosol increased by a factor of 2.1 +/- 0.7 and 2.3 +/- 1.2 between 32 and 95% RH at 467 nm and 530 nm, but there was no detectable absorption at 660 nm. Additionally, the spectral dependence of absorption by OC that was observed with filter measurements was confirmed qualitatively *in situ* at 467 and 530 nm. Closure modeling with the dynamic effective medium approximation (DEMA) refractive index model was able to capture the increasing absorption trend with RH indicating that the droplets were heterogeneously mixed while containing dispersed insoluble absorbing material within those droplets. Seven other refractive index mixing models including LVA did not adequately describe the measurements for OC. Mixing the biomass OC aerosol with select mass fractions of ammonium sulfate ranging from 25 to 36% and sodium chloride ranging from 21 to 30% resulted in an increase in light scattering and extinction with RH and inorganic mass fraction. However, no detectable difference in light absorption behavior in comparison to pure biomass OC was observed.

The main finding of this research is a measured increase in absorption with increasing RH, which is currently not represented in radiative transfer models even though biomass burning produces most of the primary OC aerosol in the atmosphere.

TABLE OF CONTENTS

1 INTRODUCTION

The quantification of aerosol optical properties is critical for the understanding of the role of aerosols in visibility [*Watson*, 2002] and in the atmosphere's radiative energy balance. Aerosol perturbation of the radiative balance may result in warming or cooling of the earth system, and this is dependent on the balance between absorption and scattering of light. Relative humidity (RH) plays an important role in the direct radiative forcing by aerosols [*Haywood et al.*, 1997; *Ramaswamy and Kiehl*, 1985] because elevated RH conditions can cause aerosol particles to uptake water, altering their size and composition and thus their interaction with light [*Orr Jr et al.*, 1958].

Many field studies have examined and observed an increase in light scattering of aerosols with increasing RH conditions. These include but are not limited to *Covert et al.* [1970], *Carrico et al.*,[1998] and *Ziegler et al.* [2010]. Detailed laboratory studies have also been conducted to analyze and quantify changes of scattering with RH for inorganic aerosols [*Tang and Munkelwitz*, 1994] or organic/inorganic mixtures [*Hansson et al.*, 1998]. Although radiative-transfer models parameterize the changes in scattering with RH according to these studies [*Boucher and Anderson*, 1995; *Ghan and Zaveri*, 2007], they frequently assume that RH has no effect on aerosol light absorption. This dependence has been less frequently investigated; a decrease in the light absorption coefficient for RH values increasing above 70% was observed in ambient measurements with a photoacoustic spectrometer [*Arnott et al.*, 2003] but this could have been caused by instrument artifacts. A decreasing absorption coefficient upon humidification was observed for wood smoke aerosols [*Lewis et al.*, 2009] and was partly attributed to a morphological change in the aerosol upon humidification. Morphological change has been found to affect optical properties of soot particles coated with sulfuric acid [*Zhang et al.*, 2008], but in the range of 10 to 80% RH, an overall absorption cross-section increase of 1.5 times was observed. Increased light absorption by a factor of up to 3.5 in comparison to dry conditions was observed for hydrophilic soot water agglomerates under saturated water vapor conditions [*E F Mikhailov et al.*, 2006]. An enhancement in absorption by mineral dust of up to 1.5 times the initial value at 80% RH was observed by *Lack et al.* [2009b].

Another facet of atmospheric aerosols that has not been thoroughly investigated is absorption by organic aerosol (OA). There are certain organic compounds that show a strong wavelength (λ) dependent absorbance near ultraviolet and blue wavelengths. Nitrated and aromatic compounds were reported as likely absorbers by *Jacobson* [1999]. Different levels of aromatization were suggested by *Bond* [2001] to explain the wavelength dependence. The absorption of organic carbon in biomass smoke was quantified with measurements by *Kirchstetter et al.* [2004]. Absorbing OA at visible wavelengths was also identified as highly oxygenated, having high molecular weight and containing one or more nitrogen atoms [*Sun et al.*, 2007].

This project entailed laboratory closure studies between predictions of optical properties, including absorption, for biomass OA mixed with inorganic material. Novel scientific components of this project included investigating:

- Changes in optical properties including aerosol light scattering, extinction, and absorption with RH
- Optical properties at high sub-saturated RH; of particular interest was the range of RH conditions between 85 and 98%, where modeled optical properties are rarely characterized by measurements
- Examination of OA from wood pyrolysis—representative of most of the primary atmospheric organic carbon—mixed with ammonium sulfate and sodium chloride

1.1 Project Objectives

The following specific objectives were proposed to DOE ASP:

1. *Assemble analytical equipment* to measure light scattering and absorption by aerosols at high sub-saturated relative humidities and at multiple visible wavelengths.
2. *Measure these optical properties* for specific organic aerosol fractions, namely oxygenated aromatic species and polymerized light-absorbing aerosol, both pure and mixed with inorganic solute.
3. *Model the optical properties* of the aerosol independent of the optical measurements and evaluate closure between measured and predicted optical properties.
4. *Identify chemical measurements* that correspond to fractions of organic carbon with distinct climate-relevant properties.
5. *Provide emission- and process-linked parameterizations* of optical properties in the form required for implementation in next-generation climate models.

2 METHODS AND DATA ANALYSIS PROCEDURES

This section provides the methods and data analysis procedures used in this project. First an overview of all the measurements is provided (Section 2.1) and the aerosol generation is discussed (Section 2.2); then, the individual measurement and methods are discussed in detail (Section 2.3 to 2.8) including applied corrections (Section 2.9) and the last sections (2.10 and 2.11) provide the approach of the performed optical closure modeling.

2.1 Overview of Measured Properties

Table 1 provides an overview of all the measured and derived properties used in this project categorized into measurements, derived variables and offline measurements. Direct measured properties included aerosol optical properties (extinction and scattering), the dry particle size distribution, environmental variables (temperature and RH) and the particle size growth factor measured with a Hygroscopic Tandem Differential Mobility Analyzer (HTDMA).

Derived properties included the light absorption by difference, the single scattering albedo, the optical growth factors of scattering, extinction and absorption and the hygroscopicity parameter κ derived from the HTDMA measurements. For the OA and mixed OA, filter measurements with quartz and nylon filters were performed. The collected mass on the quartz and nylon filters was analyzed for organic and elemental carbon (OC/EC) and ions respectively. OA filter extracts were also analyzed with nuclear magnetic resonance (NMR) spectroscopy to investigate the abundance of chemical functional groups in the organic material. More detailed descriptions of these methods are described below.

2.2 Aerosol Generation

The optical properties of six different types of aerosol were investigated in this project (Table 2).

Because the optical instrumentation was specifically adapted for this project, it was important to provide benchmarking for this instrumentation and compare results with known standards to evaluate the validity of the measurements (see section 2.2.1). The OA was generated with a temperature controlled wood pyrolysis reactor (see section 2.2.2). The OA mixed with inorganic ammonium sulfate and sodium chloride was generated by coagulating the pyrolyzed OA particles with salt particles generated with an atomizer (see section 2.2.3).

2.2.1 Instrumentation Benchmarks

The first test was conducted with ammonium sulfate as a non-absorbing benchmark for both dry and humidified conditions. This test with a well-characterized aerosol served three purposes: first, it calibrated the path length of the extinction cell under non-absorbing conditions by comparing the measured extinction with the measured scattering; second, the absolute accuracy of the instrumentation could be evaluated by an optical model for dry and wet conditions; and third, it tested the performance of the humidity measurement and control in the optical instrumentation. The second benchmark verified the accuracy of the dry light absorption measurements using mono-disperse dyed polystyrene microspheres (PSM, Thermo Scientific, XPR 1547) with a nominal diameter of 327 nm. The optical properties of these and other absorbing PSM were independently characterized by *Lack et al.* [2006]; [2009a] at the 532 nm wavelength. The third benchmark test was performed with absorbing nigrosin (Sigma Aldrich, N4754) aerosols. Nigrosin has been used previously as an absorbing benchmark under dry conditions [*Bond et al.*, 1999; *Lack et al.*, 2006; *Lang-Yona et al.*, 2009; *A. Sedlacek and Lee*, 2007]. For this work, we investigated light absorption of nigrosin as a function of RH because nigrosin is water soluble.

Ammonium sulfate, absorbing PSM and nigrosin aerosols were generated by atomizing their solutions with a constant output atomizer (TSI 3076). The atomizing pressure was set at 241 kPa (35 psig). Before dilution with particle-free dry air, the generated aerosol was dried with a silica gel diffusion dryer and charge neutralized with a custom made neutralizer which utilizes four ionizer plates (Amstat Corp., Staticmaster 2U500) with 500 μC each. The conditioned aerosol then entered a 20 L mixing chamber that smoothed concentration fluctuations. From there, the aerosol flowed into the RH-controlled instrumentation under forced draft conditions (Figure 3).

2.2.2 Primary OA from Wood Pyrolysis

A temperature controlled wood pyrolysis reactor (Figure 1) was operated to generate complex mixed primary OA. Nitrogen sheath flow was used to produce anoxic conditions in the reactor, as would occur in the middle of a wood piece. These conditions allow for pyrolysis that typically generates organic carbon, while also preventing flaming and the production of elemental carbon. This reactor was used by *Subramanian et al.* [2007] and *Y Chen and Bond* [2010] with the only difference for this project being the installation of a proportional integral differential (PID) temperature controller which allowed control within 10˚C and operating the reactor at higher temperatures. A custom annular dilution probe, connected directly to the sampling inlet above the wood pyrolysis reactor, diluted and cooled the aerosol immediately.

Chen and Bond [2010] showed that pyrolysis temperature is more important for absorptive properties than wood type. Pyrolysis at 340 - 360˚C produced a greater mass fraction of organic aerosol that is less water-soluble and more absorptive than aerosol produced at 210˚C. In this work organic carbon aerosol from red oak (*Quercus rubra*) pyrolyzed at 425˚C was investigated. The higher temperature in comparison to *Chen and Bond* [2010] was chosen because it was difficult to detect absorption at 360˚C with these *in situ* measurements in comparison to the instrumentation used by *Y Chen and Bond* [2010] which measured extracts from integrated filter measurements. Individual 2 x 2 x 2 cm (length x width x height) wood blocks were pyrolyzed for 7 minutes. The generated aerosol was sampled from the reactor at 4 SLPM and diluted with particle free dry air to a 7:1 dilution ratio. The diluted aerosol was drawn into a 208 L stainless steel storage vessel that was initially purged with nitrogen. After the pyrolysis event the vessel was disconnected from the vacuum source and reconnected in a forced draft configuration to the RH-controlled instrumentation (Figure 3). The flow rate through the storage chamber into the optical instruments ranged from 1 to 4 SLPM.

2.2.3 Primary OA from Wood Pyrolysis Mixed with Ammonium Sulfate or Sodium Chloride

The custom annular dilution probe used for sampling was used to coagulate the wood pyrolysis aerosol with the ammonium sulfate and sodium chloride particles carried by the diluent (Figure 2).

The wood pyrolysis reactor was operated the same way as for the generation of pure OC as described previously (Section 2.2.2). The OA aerosol was sampled at a flow rate of 3 SLPM above the pyrolysis reactor chimney (flow indicated in red). Ammonium sulfate and sodium chloride aerosol were generated by atomizing their bulk solutions (solute concentration = 0.1 g cm^{-3}) with a constant output atomizer (TSI Inc., 3076). The inorganic aerosol flow was then diluted and entered the mixing device annularly in cross flow to the OA. The inorganic aerosol flow was forced to bend by a 180º angle in which the carried particles experienced a stagnation point in the flow and a lower relative velocity in comparison to the velocity of the OA. The mixed flow was then drawn under turbulent conditions through the center of the dilution probe to the storage chamber. The inorganic mass fraction was controlled by changing the probe height above the pyrolysis reactor so that it sampled a differently diluted organic aerosol. “High”, “Medium” and “Low” inorganic mass fraction corresponded to probe heights of 4, 3 and 2 cm above the chimney.

2.3 Instrument Assembly

A schematic overview of the experimental setup is provided in Figure 3 and as an actual photograph (Figure 4). Details about the aerosol generation indicated at the top of Figure 3 can be found in the previous section 2.2.

Aerosol particles with an aerodynamic diameter greater than 500 nm were removed with a two stage impactor before entering the instruments [*Berner et al.*, 1979]. The switchable high efficiency particulate air (HEPA) filter bypass allowed clean air cycles for the determination of background signals without particles. The connections indicated with dashed lines varied with the type of experiment. Filters for offline analysis were only collected for OA and mixed OA aerosol experiments. The HTDMA instrument was used for nigrosin and the OA and mixed OA experiments for which the hygroscopic size growth factor had to be determined. The parallel TSI 3563 nephelometer was used for the OA and mixed OA experiments for which the concentration fluctuated with time. Details about each instrument are provided in the following sections of this report.

2.4 Optical Instrumentation

Instrumental challenges have hindered the investigation of light absorption under elevated RH conditions. Current filter-based light absorption measurement techniques have artifacts such as responses to non-absorbing aerosol and show oscillatory behavior above 80% RH [*Arnott et al.*, 2003]. Photoacoustic ambient aerosol light absorption measurements have shown a decrease in the light absorption coefficient at RH values greater than 70%. Theory indicates that some of the laser energy is consumed by mass transfer, evaporating part of the water-containing droplets and therefore lowering the apparent absorption signal by wet aerosols when compared with dry aerosols. This phenomenon could explain the observed decrease in the photoacoustic signal [*Arnott et al.*, 2003]. This interference has been theoretically characterized [*Murphy*, 2009]. One approach is to measure absorption by difference between light extinction and scattering (difference method). The difference method has been used in field campaigns [*Reid et al.*, 1998; *Virkkula et al.*, 2005; *Weiss*, 1992], for laboratory studies [*Khalizov et al.*, 2009; *E F Mikhailov et al.*, 2006; *Zhang et al.*, 2008] and as a reference method for the calibration of filter based absorption measurements [*Bond et al.*, 1999; *Weingartner et al.*, 2003]. Measurements with an extinction cell are an attractive alternative to other measurements because of the simple construction and the capacity to accommodate high relative humidities *in situ* without concerns about loss of energy to mass transfer. However, single path extinction cells have a limited sensitivity and require long path lengths for atmospheric applications. Furthermore, the difference method is prone to large uncertainties in the determined light absorption, especially at high single scattering albedos. The method developed here is currently not suitable for typical ambient aerosol concentrations. This work takes advantage of the laboratory setting to study aerosol properties, where aerosols with reproducible composition and high concentrations can be generated under carefully controlled conditions.

2.4.1 Light Extinction

The Short Path Extinction Cell (SPEC) is a modular optical extinction cell based on the design of *Virkkula et al.* [2005]. The major change from the Virkkula design is the shorter physical path length of 1.25 m instead of 6.57 m which resulted in a sensing volume of 1.75 L instead of 22.4 L and a more rigid vibration insensitive design (Figure 5). The smaller volume reduced the residence time of the sample in the cell, allowing better control of high relative humidity conditions.

The optoelectronics assembly used the electronics hardware of a 3-λ Radiance Research Particle Soot Absorption Photometer (PSAP) which is able to detect 1 part in 10^6 changes in light intensity by using integrated photon counts. The PSAP's firmware programming was not modified for use in the SPEC, but the positioning of the signal photo-detector (PD) and reference PD were altered. The setup utilizes the same PDs as the original PSAP electronics (Hamamatsu, S2387-66R). However, in the extinction cell, the PDs receive light from a beam splitter (BS, Edmund Optics, NT 45-324). The PSAP light emitting diode (LED) assembly which emits pulsed light at blue (467 nm), green (530 nm) and red (660 nm) wavelengths was used as the light source (LS). The uniformity of light across the beam path was enhanced by two holographic diffusers (HD 1, HD2, Edmund Optics, NT54-498, NT53-873) and an aperture. Dry HEPA-filtered purge air at a flow rate of 0.3 SLPM was used to keep the two achromatic lenses (L1, L2, Melles Griot, 01-LAO-238) at each end of the aerosol sensing volume clean from contamination. The purge air resulted in an effective reduction of the physical path length by 1.1 cm (0.8%) to an actual optical path length of 123.9 cm. The actual optical path length (L) of the extinction cell was determined with non-absorbing ammonium sulfate aerosol for which it was assumed that the scattering values measured with the nephelometer match the corresponding extinction values (see the dry ammonium sulfate results section). In addition, the lens purge air caused dilution of the downstream aerosol flow which was accounted for as explained later. The extinction coefficient (σ_e) at a specified wavelength was calculated from the actual optical path length and the ratio between the signal-detector photon count for clean (zero) air before and after the sample period and for sample air when aerosol is present (Equation 1). Photon counts for both zero air ($(\text{Sig. Cnt.})_{\text{Zero}}$) and sample air ($(\text{Sig. Cnt.})_{\text{Sample}}$) are the respective ratios to the measurements at the reference detector (Ref. Cnt.) to account for signal drift.

$$\sigma_e(\lambda) = -\frac{1}{L}\ln\left(\frac{\left(\text{Sig. Cnt.}(\lambda)/\text{Ref. Cnt.}(\lambda)\right)_{\text{Sample}}}{\left(\text{Sig. Cnt.}(\lambda)/\text{Ref. Cnt.}(\lambda)\right)_{\text{Zero}}}\right) \quad \textbf{(1)}$$

The extinction sensitivity and detection limit were determined by recording the signal and reference PD counts under steady conditions for dry clean air, respectively. The uncertainties of the zero and sample period were added in quadrature to determine the uncertainty of the extinction. The extinction detection limit was set to be three times the standard deviation of the obtained extinction noise.

2.4.2 Light Scattering

A wavelength modified TSI 3563 nephelometer was used to measure light scattering and backscattering at three wavelengths (470, 530, and 660 nm). Under normal sampling conditions, heating within the nephelometer can increase the temperature as much as 4.5°C, thereby altering the RH in the nephelometer's sample volume. Several modifications were employed to reduce heating and optimize the instrument's ability to measure light scattering at high RH:

1) Exchanged halogen lamp to a version with reduced wattage and thinner filament (General Electric, Q20MR16C/CG40˚)
2) Installed a hot mirror (Edmund Optics, 46388) in front of the lamp to eliminate thermal radiation into the sampling volume of the instrument.
3) Separated electronics from the instrument body [*Heintzenberg and Erfurt*, 2000]

4) Increased lamp ventilation with external blowers and reduced power input to lamp [*Carrico et al.*, 1998]

These modifications reduced the sample heating from the original 4.5°Cto 0.5 +/- 0.1°C, which made scattering measurements up to 95% RH possible. Observed nephelometer sample RH reductions due to the heating were 2.6% for an inlet RH of 80% and 3.2% for an inlet RH of 95%. In addition the optical band pass filters in front of the photomultiplier tubes were exchanged with new filters with peak wavelengths of 470, 530, and 660 nm (Edmund Optics, NT-62). This modification allowed the comparison between the scattering and extinction values without wavelength corrections to reduce uncertainty in the accurate determination of light absorption by difference.

The reduced lamp power and the hot mirror resulted in decreased signal relative to noise which made the standard calibration with air and carbon dioxide (CO_2) more challenging, especially at 660 nm. Therefore, longer calibration averaging times were chosen and sulfur hexafluoride (SF_6, Matheson Inc., 99.95% purity) was used as the high span gas. The calibration was verified by comparing measured CO_2 and SF_6 Rayleigh scattering values with values determined by *Bodhaine* [1979] at the specific wavelengths and in comparison to an unmodified nephelometer (TSI 3563, Figure 4). The scattering sensitivity and detection limit of the modified instrument was determined with clean air similar to the method described by *Anderson et al.* [1996]. To account for scattering by water vapor and wall scattering at elevated RH values, background scattering measurements were performed at 70 and 90% RH which corrected the background scattering signal by 0.7 and 1.5%, respectively [*Carrico et al.*, 2000].

An additional nephelometer (TSI 3563) was operated in parallel to the sample flow (see dashed line in Figure 3). This measurement was used to account for decreasing aerosol concentrations due to dilution of the storage chamber by the forced draft flow in the wood smoke experiments. Additional discussion about the dilution correction can also be found in 2.10.5.

2.5 Relative Humidity Measurement and Control

The RH in the system was controlled by maintaining a constant dry bulb temperature and varying the dew point temperature. The dew point was set by an annular humidifier which controls water vapor diffusion through a tubular Gore Tex® membrane [*Carrico et al.*, 1998]. The RH instrumentation included two capacitance-based RH sensors (Vaisala, HMP 230) and two chilled mirror-based dew point sensors (General Eastern, Hygro M1). Four thermocouples (Omega, Inc.) for dry-bulb temperature measurements were distributed in the system in addition to the existing dry-bulb temperature measurement within the nephelometer (T_{sample}). A heat exchanger was installed after the humidifier to reduce the difference in dry bulb temperatures between the initially humidified sample flow and within the optical instrumentation.

One capacitive-based RH and one dew point sensor were sent to their manufacturers for accredited calibrations. These sensors served as a standard for the remaining two sensors which were calibrated in-house over five temperature controlled saturated salt solutions (K_2CO_3, NaCl, KCl, KNO_3 and K_2SO_4) over a range of 43.2 to 97.4% RH (at 20ºC). The temperature calibrations of the thermocouples were verified against a National Institute of Science and Technology (NIST) reference thermometer with ice and boiling water. However, no adjustments were made since the recorded values were within 0.15°C of the reference. The overall performance of the humidity sensors was checked by placing them at their actual sampling location and varying the set-point of the humidifier (See humidity sensor performance results section).

2.6 Particle Sizing

Aerosol number concentrations and size distributions were measured upstream of the humidifier with a Scanning Mobility Particle Sizer (SMPS, TSI Instruments, 3934). The SMPS aerosol flow was at 0.3 LPM and the sheath flow was 2.4 LPM. The sizing accuracy of the SMPS system was evaluated by measuring 200 nm and 350 nm mono-disperse polystyrene latex spheres (Thermo Scientific, 3200A/ 3350A) and comparing the resulting measured diameters reported by the SMPS. The electrostatic classifier used in the SMPS system was operated with HEPA filtered recirculating sheath air flow.

2.7 Hygroscopic Tandem Differential Mobility Analyzer Measurements

Research for measuring aerosol volatility and hygroscopicity with differential mobility analyzers has been performed successfully for decades [*McMurry and Stolzenburg*, 1989; *Rader and McMurry*, 1986; *Swietlicki et al.*, 2008]. An overview of the HTDMA used in this research to measure the hygroscopic particle size growth factor as a function of RH is provided in Figure 6.

The poly-disperse aerosol flow indicated in red is first brought to a defined charge distribution with a custom made charge neutralizer which utilizes four ionizer plates (Amstat Corp., Staticmaster 2U500) with 500 μC each. A selector DMA (TSI 3071) is used to select a specific aerosol size from the distribution as the initial dry diameter. This dry diameter is then passed through the humidifier and measured by a scanning DMA to determine the particle size growth. The sheath air flows in both, the selector and scanning DMAs are recirculated by pumps (P1, P2) and controlled by needle valves in combination with mass flow meters (MFM). The only difference in the sheath flows is the use of a PolyTetraFluoroEthylene (PTFE) filter in the scanning DMA in contrast to the standard glass fiber HEPA filter in the selecting DMA to avoid the uptake of water by the filter in the humidified air stream. The humidifier system is a smaller version of the system described in section 2.5 in which the water surrounding the Gore Tex® membrane is recirculated by a peristaltic pump (WP). The temperature and RH in the scanning DMA is monitored by three sensors (Sensirion, SHT 75) for which the location is indicated in Figure 6. An additional Sensirion RH/T sensor is used to monitor the inlet of the humidifier. The sensors were calibrated by comparing their measured values with the Vaisala RH/T sensor and the GE dew point sensor used in the optical instrumentation that were sent to their manufacturers for accredited calibrations. This ensured an accurate inter-comparison between the optical instrumentation and the HTDMA and correlated the absolute RH/T accuracy to the NIST accredited calibration by the sensor manufacturers. The result for the sensor calibration can be found in section 3.1.3 for a range of RH between 2 and 97.5%. For the checking of the overall performance of the HTDMA system, ammonium sulfate was used as a calibration aerosol because its growth data are readily available in the literature, e.g., *Tang and Munkelwitz* [1994]. The performance test results are provided in section 3.2.1.

2.8 Offline Analysis of Collected Aerosol Filter Mass

For the OA and mixed OA experiments, two parallel 47mm filter packs (URG-2000-30RAF, URG Corp, Chapel Hill, NC) were used to collect filter samples for mass measurements of OC/ EC and inorganic ions. A quartz fiber filter (Tissuquartz 2500, Pall Inc.) was used to collect aerosol for the OC/EC determination whereas a nylon membrane filter (Nylasorb 66509, Pall Inc.) was employed for the determination of inorganic ion mass.

2.8.1 OC/EC Analysis

OC and EC mass on both front and back quartz filters were analyzed with a Sunset Laboratory OC/EC Analyzer (Sunset Laboratory, Tigard, OR) using the thermal-optical-transmittance (TOT) method. The instrument was operated according to the procedure described in *Subramanian et al.* [2007] with a temperature profile based on NIOSH Method 5040 [*NIOSH*, 2003]. Primary OM was determined by forcing the measured OC mass from the OC/EC analysis to match the mass determined by gravimetric analysis without the determined ionic masses. Therefore the OM/OC ratio which quantifies this correction is also reported in the results.

2.8.2 Inorganic Mass Fraction

The inorganic mass collected on the nylon filters was dissolved with 50 ml of nano-pure water. The filter solution was sonicated for 45 minutes to ensure that the collected ionic mass dissolves from the filter. The solutions were then filtered with a 0.45 μm PTFE membrane filter (Flouropore, Pall Inc.) to prevent fouling in the ion chromatography instrument (ICS-2000, Dionex Inc.) which was used for the anion analysis. Two samples for which the anionic concentration in solution was more than 5 ppm_m were additionally diluted by a factor of 10 to prevent instrument overloading. The Ca, Mg, K, and Na cations were analyzed by using an Inductively Coupled Plasma Optical Emission Spectroscopy (ICP-OES) instrument, (Vista Pro, Varian Inc.), whereas NH_4, PO_4 concentrations were measured by using colorimetry on a flow-injection analyzer (FIA) instrument (QuikChem 8500 Series 2, Lachat Inc.).

2.8.3 Nuclear Magnetic Resonance Spectroscopy

We used nuclear magnetic resonance (NMR) spectroscopy to probe the functional groups associated with absorbing aerosol. There is evidence that larger aromatic clusters, or possibly conjugated carbon double bonds, are the cause of light absorption [*Sun et al.*, 2007]. However, standard proton (^{1}H) NMR cannot detect these conjugated bonds if no protons are attached to them. Both ^{1}H and ^{13}C nuclear magnetic resonance (NMR) spectroscopy were therefore utilized to determine functional groups in the OC extracts.

The sample amount required in NMR experiments is much higher than that for the optical and other filter extract measurements, usually more than 20 mg in 0.6 mL solvent. New OC samples were generated for NMR analysis by pyrolyzing multiple pieces of wood at temperature settings with the "low" setting corresponding to 300°C and the "high" setting to 425°C. The entire filter was then extracted with solvents (15-17 mL). Extracts normally contained around 30 mg of carbon. The extract was then dried in a dry-bath incubator (Isotemp, Fisher Scientific) at 50°C to evaporate all the solvents. Dried OC was redissolved into 0.6 mL deuterium solvent for NMR analysis. Deuterium dimethyl sulfoxide (DMSO-d_6) was used as the solvent because of its capability to dissolve a large amount of sample in a very small volume of solvent. Deuterium methanol, acetone and water were tested, but were not suitable for this project because precipitation was observed for the high-concentration sample in these solvents due to the limitation on solubility.

The analysis was performed at the NMR lab in the School of Chemical Science at the University of Illinois at Urbana-Champaign. Liquid ^{1}H and ^{13}C NMR spectra were acquired on a Varian Unity 500 at the frequency of 500 MHz for ^{1}H and 125.7 MHz for ^{13}C. Experiments were carried out at 35°C to avoid the freezing point of DMSO (19°C). 128 transients were taken for ^{1}H NMR spectra and around 5000 transients were taken for ^{13}C NMR.

All NMR spectra were divided into several spectral regions based on the chemical shift of ^{1}H and ^{13}C atoms in different functional groups, as shown in Table 3 and Table 4. The regions were determined based on *Tagliavini et al.* [2006] and *Graham et al.* [2002] for ^{1}H NMR and *Sannigrahi et al.* [2006] and *Duarte et al.* [2007] for ^{13}C NMR with slight modifications according to the solvent peaks. The integrated peak areas in each region were determined and solvent residual peaks were subtracted. Data processing and peak integration (including residual peak subtraction) were carried out using the MestReNova software (Mestrelab Research, Santiago de Compostela, Spain). The software returns absolute peak areas relative to a reference peak. Percentage peak areas of individual regions were then calculated by dividing their areas by the total spectra peak area of the sample. The percentage peak areas are a semi-quantitative measure of the relative contributions of different functional groups to the OC present in the sample because the spectral range of each function group is only an approximate estimate. These values allow us to understand the prevalence of certain functional groups in OC composition.

Recycle delay (d_1) is a critical operation parameter for NMR experiments. During the recycle delay, the excited sample returns to its equilibrium state. Too short d_1 will result in inaccurate results due to the loss of signal because the sample is not fully relaxed for the next excitation, while too long d_1 will waste of spectrometer time. The optimized recycle delay was determined with a trial-and-error method for both ^{1}H and ^{13}C NMR. A series of four experiments was performed on a typical methanol extract, in which the recycle delay was set to 1 s, 3 s, 5 s and 10 s. The optimized d_1 was determined when the percentage peak area of each functional group was constant. In the optimization experiments, 128 and 256 scans were taken for H and ^{13}C NMR respectively. Optimized recycle delay was determined by comparing the percentage peak area of each region for different d_1 (Figure 7).

For both ^{1}H and ^{13}C NMR, the change of percentage peak areas was less than 3% when recycle delay was increased from 5 s to 10 s. We therefore used a d_1 of 5 s for the samples. For ^{13}C NMR, regions of 160-190 and 190-230 were not included because the areas for those two regions were below detection limit.

2.9 Instrument Corrections and Data Analysis Procedures

2.9.1 Corrections to Extinction and Scattering

The measured extinction and scattering coefficients were corrected to standard laboratory temperature (298.15 K) and pressure (1013.15 mbar). Additionally the scattering coefficient was corrected for the dilution of the aerosol flow, $Q_{Aerosol}$, caused by the lens purge flow of the extinction cell, Q_{Purge}, shown in Equation 2.

$$\sigma_{sp} = \sigma_{sp}\left(\frac{Q_{Aerosol}+Q_{Purge}}{Q_{Aerosol}}\right) \quad (2)$$

The nephelometer's angular truncation was corrected for sub-micrometer diameter ammonium sulfate aerosol particles [*Anderson and Ogren*, 1998]. For absorbing aerosol with single scattering albedo $\omega < 0.9$, the truncation correction approach of *Bond et al.* [2009] was followed; the correction was calculated with an assumed refractive index and Mie theory based on the measured particle size distributions.

2.9.2 Determination of Actual RH in Scattering Volume

Because of the slightly elevated temperature in the nephelometer, scattering is measured at a different RH than the rest of the system. The actual RH in the sensing volume of the nephelometer was calculated from the average of the two dew-point temperature values measured upstream and downstream of the nephelometer ($T_{DP,Ave}$) with the T_{sample} values provided by the nephelometer (Equation 3).

$$RH=100\left(\frac{\exp\left(\frac{\beta T_{DP,Ave}}{\lambda_w+T_{DP,Ave}}\right)}{\exp\left(\frac{\beta T_{Sample}}{\lambda_w+T_{Sample}}\right)}\right) \quad \textbf{(3)}$$

In Equation 3, $\beta = 17.62$ and $\lambda_w = 243.12$ K [*WMO*, 2008]. This procedure was observed to be the most accurate to determine the RH within the nephelometer's sensing volume due to sample heating within the nephelometer [*Carrico et al.*, 1998; *Koloutsou-Vakakis et al.*, 2001; *Kus et al.*, 2004].

2.9.3 Determination of Light Absorption and Single Scattering Albedo

The extinction measurements covered the entire range of RH values experienced by the nephelometer, but did not occur at exactly the same RH value due to the nephelometer heating. Therefore, the extinction coefficient that would have been measured at the RH within the nephelometer was inferred by using a cubic spline interpolation of RH values above and below the RH for the extinction cell ($\sigma_{ep,int}$). The light absorption coefficient σ_{ap} and ω at the RH of the nephelometer were calculated from the interpolated extinction coefficient (Equations 4 and 5).

$$\sigma_{ap}(RH)=\sigma_{ep,int}(RH)-\sigma_{sp}(RH) \quad \textbf{(4)}$$

$$\omega(RH)=\frac{\sigma_{sp}(RH)}{\sigma_{ep,int}(RH)} \quad \textbf{(5)}$$

The absolute uncertainties for light absorption were calculated by adding the uncertainties of the extinction and scattering measurements in quadrature.

2.9.4 Particle Sizing corrections and HTDMA Inversion

Particle Sizing

The aerosol instrument software (Version 9.0, TSI Inc.) was used to collect and process the data from the SMPS system. The embedded multiple particle charge correction inversion algorithm from the TSI aerosol instrument manager software was to correct the instrument for multiple charged particles.

HTDMA

From the H-TDMA results the size growth factor f(RH)Dp can be calculated as shown in Equation 6

$$f(RH)Dp = \frac{CMD(RH)}{CMD(dry)} \quad \textbf{(6)}$$

where CMD is the count median diameter of the size distribution at the chosen RH and dry conditions, respectively. The dry and humidified CMD values were taken from the TSI inversion software. To verify the accuracy of our data analysis the H-TDMA data were also analyzed using TDMAinv, and inversion software designed by *Gysel et al.* [2009] which returns f(RH)Dp and its standard deviation. The derived f(RH)Dp results were fitted using the κ-Köhler model [*Petters and Kreidenweis*, 2007] to obtain a continuous curve according to the work of *Carrico et al.* [2008], except that a constant κ for all RH is used in this study.

2.10 Optical Closure Evaluation

Modeling optical properties from the measured size distributions and known chemical properties of the particles allows an independent verification of directly measured optical results. A conceptual overview of the modeling approach is shown in Figure 8.

A computer program based on the Mie–Lorentz light scattering (BHMIE) code of *Bohren and Huffman* [1983] was used to calculate aerosol optical properties during both dry and humidified aerosol experiments. Particles were assumed to be homogeneous spheres of uniform density for dry and hydrated conditions. The size growth factor was determined from the HTDMA data with the procedures described in section 2.9.4. The hydrated size distributions as a function of RH were calculated by assuming that all of the particles in each size bin grow equally and the dry aerosol particle number concentration is conserved under humidified conditions (no coagulation or particle loss). The refractive index at different RHs was calculated using different formulas for mixtures commonly used in the literature. Specific details for the mixing rules for each aerosol type are explained later. The model returned values for σ_{ep}, σ_{sp}, and σ_{ap} at different RH, and with this information the optical growth factors f(RH) for extinction scattering were calculated as described in Table 1.

2.10.1 Refractive Index

For modeling the optical properties of ammonium sulfate, nigrosin, OA and mixed OA, the refractive indices are needed as well as the refractive index of their mixture with water at different RH. The refractive index of the dry substances can be deduced with the measured extinction, scattering, and size distribution values, plus the Mie-Lorenz model. For the refractive index of aerosols at different RH (i.e., aerosol plus water) different refractive index mixing rules were used to determine which one gave the best closure between model results and measurements.

The mixing rules used are: the linear volume average (LVA) or *Biot*, widely used due to its simplicity, with the caveat that it should be used for quasi-homogeneous mixtures in which refractive indices of components are similar [*Liu and Daum*, 2008]; the Lorentz-Lorenz mixing rule is more general [*Liu and Daum*, 2008], although it still assumes an ideal mixture (i.e., it does not take into account changes in volume [*Mehra*, 2003; *Postigo et al.*, 2008]. The Maxwell-Garnett mixing rule [*Aspnes*, 1982] considers a spherical inclusion embedded in a medium with different dielectric properties, the problem being deciding which substance is the medium and which the inclusion. Both configurations were tested to compare. Bruggeman [*Aspnes*, 1982]

proposed that neither phase should be given preference, that the inclusion should be considered as being embedded in the effective medium itself. A further configuration tested was core-shell, with the substance (here Nigrosin or OA) forming an insoluble core surrounded by a shell of water [*Bond et al.*, 2006]. Finally, the dynamic effective medium approximation (DEMA) model [*Chylek and Srivastava*, 1983; *Jacobson*, 2000], which assumes a composite media with absorbing inclusions, was used. An illustration of the LVA and DEMA mixing rule is provided in Figure 9.

All mixing rules require knowledge of the volume fraction of water v_w and solute v_s, which were calculated as shown in Equations 7 and 8.

$$v_w = f(RH)Dp^{-3} \quad \textbf{(7)}$$

$$v_w = 1\text{-}f(RH)Dp^{-3} \quad \textbf{(8)}$$

based on the assumption that volume additivity is valid.

2.10.2 Modeled Uncertainties

Upper and lower estimates of the optical properties were calculated to describe the range of reasonable values. For this, the standard deviation of f(RH)Dp was used to calculate larger and smaller size distributions (i.e., each size bin was increased or decreased by the standard deviation), and optical properties were calculated again with those modified size distributions, providing upper and lower estimates of the optical properties. Other uncertainties were added in quadrature to these values: 1% due to CPC counting, 2% due to unknown refractive index, and 3% due to SMPS bin width (these values were obtained from a sensitivity analysis of these parameters). An f(RH)Dp uncertainty value of 0.03 was used from analysis of several H-TDMA experiments.

2.10.3 Ammonium Sulfate Modeling Details

The effect of the dry particle shape was neglected for AS because the correction for non-sphericity is small (< 2%) [*E Mikhailov et al.*, 2009] for the aerosol types used in this study. For the humidified AS experiments, refractive index and density as a function of RH were taken from *Tang and Munkelwitz* [1994] and *Tang* [1996]. For the HTDMA verification, f(RH)Dp curves were calculated using the models of *Tang* [1996] and the Köhler model as explained by *Rose et al.* [2008], the difference being that the former does not incorporate the surface tension (Kelvin) effect while the latter does. These theoretical results were compared to the H-TDMA GF as a benchmark study.

Optical properties were calculated using the Mie-Lorenz model and all refractive index mixing rules mentioned earlier, except for the Core-Shell and DEMA models since AS is soluble in water.

2.10.4 Nigrosin Modeling Details

The measured extinction, scattering, and size distribution values were compared to Mie-Lorenz model predictions, and the refractive index of nigrosin was back-calculated from this comparison. H-TDMA results allowed calculating the hygroscopicity parameter (κ) and with this information the absorption coefficient can be modeled and compared with measured σ_{ap} values.

All mixing rules were used in this case to assess their importance in modeling the optical properties and their agreement with derived measured results.

2.10.5 OA Modeling Details

The refractive index of OA, the extinction, scattering and absorption coefficients, and their uncertainties were determined in the same way as explained for nigrosin, except to use a correction factor to take into account changes in solute concentration. In the case of AS and nigrosin, the atomizer provides stable size distributions throughout the experiments. In the case of OA, the size distribution changes with time as the sampling reduces the concentration in the storage vessel, and it is not obvious *a priori* that one pyrolysis experiment can be reproduced since there are several parameters to take into account (e.g., composition of each wood block, temperature fluctuations). To correct for the change in concentration with time, in each experiment, the dry and humidified extinction and scattering values were measured, then humidified optical results were normalized by the ratio between the dry scattering of such experiment and the lowest dry scattering(Equation 9),

$$\sigma^{j}_{s,\,\text{corrected}}\left(\text{RH}\right) = \frac{\sigma_s\left(\text{RH}\right)}{\left(\sigma^{j}_{s,\text{dry}} / \min \sigma_{s,\text{dry}}\right)} \qquad \textbf{(9)}$$

where $\sigma^{j}_{s}(\text{RH})$ is the scattering coefficient of experiment *j* at a given RH, $\sigma^{j}_{s,\,\text{corrected}}(\text{RH})$ is the coefficient corrected for the change in concentration, $\sigma^{j}_{s,\text{dry}}$ is at dry conditions, and $\min \sigma_{s,\text{dry}}$ is the minimum scattering at dry conditions. The same procedure was used for extinction and absorption, although the correction factor (the denominator) remains the same (i.e., calculated from scattering). The correction factors for experimental results were calculated from measured scattering values, while for modeling results the correction factors were calculated from the modeled scattering values.

3 RESULTS

The results are presented in four sections: 1) instrumentation performance and calibration, 2) benchmark testing, 3) humidified organic aerosol from wood pyrolysis, and 4) humidified mixed organic aerosol from wood pyrolysis results. While the primary purpose of this work was to examine absorption by organic and mixed organic matter at high RH, benchmarking was necessary to provide confidence in the developed instrumentation.

3.1 Instrumentation Performance and Calibration

3.1.1 Optical Instrumentation Sensitivities and Detection Limits

The root mean square (RMS) noise values of the measured extinction and scattering coefficients of particle-free air as a function of wavelength and sample averaging time are shown in Figure 10.

Between the averaging time of 4 and 120 s, the RMS noise of both instruments follows a typical white noise behavior and decreases linearly with the square root of integration time. The lowest noise for the extinction cell is reached after an averaging time of 120 s to 300 s, after which the noise begins to increase due to low frequency drift. The main cause of the drift is temperature fluctuations that affect the stability of the signal and reference PDs. The lowest noise level for the extinction coefficient was observed to be 19.1 Mm^{-1} (467 nm), 21.5 Mm^{-1} (530 nm) and 35.1 Mm^{-1} (660 nm) at an averaging time of 256 s. At the same averaging time, these values correspond to an extinction detection limit of 57.3 Mm^{-1} (467 nm), 64.5 Mm^{-1} (530 nm) and 105 Mm^{-1} (660 nm) if the lowest acceptable detectable signal to noise ratio is 3. The noise and approximate detection limits of the modified TSI nephelometer do not show a drift with time after 300 s and its noise levels stabilize at 0.58 Mm^{-1} (470 nm), 0.27 Mm^{-1} (530 nm) and 2.5 Mm^{-1} (660 nm) at an averaging time of 128 s.

3.1.2 Modified Nephelometer Calibration and Performance

The nephelometer calibration was checked by measuring the Rayleigh scattering of the calibration gases air, CO_2 and SF_6 and comparing the measured values with theoretical values theory. In addition, the performance of the modified instrument was evaluated by comparing the measured particle light scattering coefficient for ammonium sulfate aerosol with wavelength-adjusted values from an unmodified nephelometer (Figure 11). Panel a) shows the measured Rayleigh scattering values for air (used as zero), and CO_2 and SF_6 (used as spans). The error in the wavelengths are the uncertainties of the band pass filters reported by the vendor, and the error bars for the scattering values are the standard deviations from a 120 s sample period. Both the standard and modified instruments agree well with the theoretical values obtained by *Bodhaine* [1979] which are indicated by dashed lines for each gas.

Figure 11b) shows the agreement of the modified nephelometer with the wavelength-corrected unmodified instrument for different ammonium sulfate aerosol concentrations. The scattering coefficients measured at 450, 550 and 700 nm were interpolated to the wavelengths of the modified instrument (470, 530 and 660 nm) assuming a constant Ångström exponent within the wavelength intervals. The error bars in the vertical direction indicate the measured standard deviations for a 120 s sample averaging time. The error bars in the horizontal direction include interpolation uncertainty values of 1.8% (470 nm), 1.5% (530 nm) and 1.1% (660 nm) from *Virkkula et al.* [2005] in addition to the measured standard deviation of the sample. The instruments show an excellent linear agreement with a maximum deviation of 1.4% at 530 nm,

which is within the uncertainty of the wavelength interpolation. We conclude that the modifications to the nephelometer do not reduce the accuracy of the scattering measurement.

3.1.3 Humidity Sensor Performance

The accurate determination of RH at multiple points is critical to ensure that different measurement techniques measure the same aerosol. Figure 12 shows the agreement among the RH sensors placed in the optical instrumentation at different controller set points, which are indicated with a dashed line. The whiskers show the minimum and maximum values, the box indicates the lower and upper quartiles and the mean value is given as a small solid circle.

The RH values for the dew-point sensors (DP1 and DP2) were determined by using the co-located dry-bulb temperature measurements. The data are from sampling periods of 180 s after equilibration after each humidity change. The sampling system reaches stable RH equilibrium in less than 45 s for RH values below 85% and up to 180 s for RH values of 90 and 97.5%. All sensors show an agreement within their manufacturer specified range of +/- 2% RH for all measurements and the obtained mean values all lay within 1.7% RH. The largest discrepancy was observed for the highest RH set point which can be attributed to several reasons, including small temperature gradients between sensor locations and issues with sensor technology at high RH values. The polymers used in capacitance based measurements become water saturated [*Z Chen and Lu*, 2005] and the uncertainty in the calculated RH values from the dew point sensors becomes larger [*Gates*, 1994].

The agreement of HTDMA RH sensors with the average of the two NIST accredited sensors is shown in Figure 13a) for RH values between 2 and 97.5%. Figure 13b) shows the residuals of the individual sensors to the accredited standard since there is almost no observable difference between the measured and reference RH values (Figure 13a).

The residuals shown in Figure 13b) indicate a good overall agreement of the sensors within 1% RH of the reference values. There is some calibration error dependency observable with increasing RH. At 97.5% accredited reference RH the HTDMA sensors measure up to 0.8% higher than the reference sensor. This discrepancy can be attributed to similar reasons as mentioned above for the capacitance based sensors at high RH. This inter-comparison is not a measure of absolute accuracy since the accredited reference RH is only certain within a range of +/- 1.5% RH for RH values between 10 and 90% and +/- 2.5 RH for sub-saturated RH values outside of 10 and 90% RH. Therefore an additional benchmark of the HTDMA system with an aerosol of known hygroscopic properties, in this case AS described in Section 3.2.1, is essential to verify the overall performance of the system.

3.2 Benchmark Testing

3.2.1 Ammonium Sulfate

Well researched optical and thermodynamic properties make AS an ideal benchmarking compound for the optical measurements under dry and humidified conditions and to evaluate the performance of the HTDMA system.

Optical Measurements

As previously mentioned, AS was used as a non-absorbing benchmark to verify the agreement between light scattering and extinction. Additionally this benchmark allowed an accurate evaluation of optical closure.

Dry Scattering and Extinction Agreement

Ideally, under non-absorbing conditions the measured extinction values equal the measured scattering values. In this work non-idealities were observed and the measured extinction values were corrected to the measured scattering values by correction factors determined by linear regressions. The regression coefficients to determine the corrected extinction values ($\sigma_{ep,corrected}$) based on measured scattering values ($\sigma_{sp,measured}$) for 21 aerosol concentrations ranging from 400 to 3,000 Mm^{-1} at three wavelengths are provided in Table 5.

The regression coefficients for matching the measured extinction values with the measured scattering values show slight wavelength dependence and offset, but the intercept values are within the noise of the instrument. The deviation from the ideal slope of unity at different wavelengths can be attributed to uncertainties in wavelength filters and light sources, and alignment of light sources. (LEDs at each wavelength do not have identical locations and therefore are not at the same focal point.) All measured extinction results are corrected with these regression coefficients, which implies that we relate the accuracy of our extinction measurements to the accuracy of the nephelometer.

Dry Scattering Closure with Mie Model

The measured scattering values were compared with values modeled using measured size distributions to verify the accuracy of the scattering measurement (optical closure). A linear regression between the measured and modeled scattering values for 21 aerosol concentrations ranging from 400 to 3,000 Mm^{-1} is shown in Table 6.

Results from the Mie model and the scattering measurements match with a maximum deviation (over prediction of true value) of 6% at 660 nm. This agreement is comparable to other closure studies for inorganic aerosols [*Anderson et al.*, 1996].

Optical Properties as a Function of RH

Figure 14 shows humidograms of scattering and extinction coefficients for ammonium sulfate for all three wavelengths. Experimental values are presented as symbols. Modeled values with their uncertainties are shown as solid and dashed lines, respectively. The abrupt increase in scattering and extinction values is attributable to deliquescence of the aerosol. This appears to occur at lower RH values for scattering in comparison to extinction and theoretical values. Such reduction in the apparent deliquescence values is caused by the heating of the nephelometer. For a narrow range of RH (< 5%), particles deliquesce upstream of the nephelometer and then lose water due to reduced RH conditions within the nephelometer's sensing volume to a value below the deliquescence RH. The particles remain as droplets in a metastable state and make it appear that deliquescence occurs at RH values below thermodynamic values reported for AS.

The instrumentation is able to measure light extinction at RH up to 98.5% and there is good agreement with the modeled scattering values up to 95% RH. The maximum RH of the scattering measurement (95%) is lower than that of the extinction due to the heating in the nephelometer. Particle losses and uncertainties in the RH measurement may explain the mismatch between measurement and modeled results at high RH. However, the extinction and scattering measurements agree well, so particles are not lost between the extinction cell and the nephelometer up to 95% RH. Therefore, particle losses may affect the model-measurement comparison and the apparent growth factor, but not the ability to measure single-scattering albedo values up to 95% RH.

HTDMA Performance Evaluation

Figure 15 shows the measured size growth factor data f(RH)Dp as a function of RH for AS particles with a dry diameter of 100 nm. The red and blue lines represent the modeled values by a full Köhler model and the model proposed by *Tang* [1996]. The vertical error bars are the values provided by the TDMAinv software, whereas the horizontal error bars represent the range of the three RH sensors within the HTDMA. The modeled values are well within the uncertainties of the measured data indicating good HTDMA system performance in terms of precision and absolute accuracy.

3.2.2 Dry Absorbing Microspheres

Because optical properties of the absorbing PSM have been previously determined at the 532 nm wavelength [*Lack et al.*, 2006; *Lack et al.*, 2009a], they were used as a benchmark to demonstrate that our instrumentation could accurately measure light absorption. Figure 16 shows the relationship between the measured scattering and extinction values to retrieve ω values by means of a linear regression at each wavelength. The linear fit is indicated as a dashed line. The error bars correspond to measured standard deviations for an averaging time of 120 s.

The measured ω value of 0.86 +/- 0.02 at 530 nm shows good agreement with Lack's reported ω value of 0.86 +/- 0.02 at 532 nm [*Lack et al.*, 2009a]. This result verifies the accuracy of the optical method to quantify ω values under dry conditions.

3.2.3 Nigrosin

Nigrosin is a water soluble compound and therefore provides an opportunity to examine the dependence of light absorption on RH.

Hygroscopic Size Growth Factor

Figure 17 provides the results of the measured hygroscopic size growth factor which was used to model the optical properties. The figure indicates that nigrosin is hygroscopic with a diameter growth factor of 1.37 at 91.6% RH in comparison to dry conditions. At 91.6% RH there is almost 1.6 times more solvent (water) present in the aerosol than solute (nigrosin). The derived κ parameter was found to be 0.165 +/-0.003, which is in the range of values for levoglucosan, glutamic acid, and glutaric acid [*Petters and Kreidenweis*, 2007].

Optical Measurement

Figure 18 provides the measured and modeled optical properties for nigrosin at all measured wavelengths. Extinction and scattering error bars are measured standard deviations for an averaging time of 120 s. Error bars for absorption are the pooled standard deviations of the measured scattering and extinction values. Error bars for RH are the absolute measurement uncertainties of the RH measurements specified by the sensor manufacturers. The modeled values were obtained with the linear volume average mixing rule of water and nigrosin. The refractive indices (m = n +i k) were 1.6 + i0.25 at 467 nm, 1.6 + i0.4 at 530 nm, and 1.71 + i0.48 at 660 nm which are slightly lower for the real part (n), and higher for the imaginary part (k) in comparison to literature values [*Lack et al.*, 2006; *Lang-Yona et al.*, 2009] and *Garvey and Pinnick* [1983].

Extinction and scattering increase with increasing RH values due to water uptake, which results in larger aerosol size. The derived light absorption coefficient is highest at 530 nm, followed by 660 nm and 467 nm. A similar wavelength dependence has been reported for bulk

measurements of nigrosin solutions [*Arthur Sedlacek and Lee*, 2006]. As RH increases, there is an increase in light absorption and an increase in single scattering albedo. The absorption growth factor ($f(RH)\sigma_{ap}$), described by (σ_{ap} (RH = 95% RH)/σ_{ap} (RH = 38%)), is 1.22 +/-0.06 at 530 nm wavelength (panel d). Overall, a good agreement with the linear volume average mixture Mie model for all optical coefficients is observed up to RH = 90%. Above 90% RH all the modeled coefficients tend to be higher than the measurements which could be explained by particle losses, the extrapolated, uncertain size growth at these RHs and uncertainties in the RH measurement overall. Particle losses in the humidifier can also explain the good measurement and model agreement for the single scattering albedo (ω) event though there is slight disagreement for $f(RH)\sigma_{ap}$ shown in d) at 95% RH. An explanation for the overall discrepancy between the modeled and measured growth pattern could be the usage of a constant κ parameter at all RHs which might be invalid for concentrated solutes present at RH values < 85%.

3.3 Organic Aerosol from Wood Pyrolysis

Nigrosin and absorbing PSM have no apparent relevance to the earth's atmosphere but served as benchmarks to build confidence in the ability of the instrumentation to measure atmospherically relevant, biomass related OA. This section first provides the results for the chemical composition analysis of the studied particles, then the results for the hygroscopic properties are provided and last the measured optical properties and closure analysis are discussed.

3.3.1 OA Composition Analysis (Filter Measurements)

Since OC generated by the pyrolysis of biomass is a complex mixture of various compounds, the material was analyzed chemically to understand the linkage between chemistry, hygroscopicity and optical properties. Relevant for hygroscopic properties is the amount of water active substances that are present in the particles. Table 7 provides the mean and standard deviation for the composition analysis of organic mass (OM) and inorganic ion mass measurements for three independent filters. The determined OM/OC correction factor of 1.68 ± 0.09 is within the range of previous studies; Turpin and Lim (2001) reported values ranging from 1.4 to 2 depending on sources and atmospheric processing. Hand et al. (2010) reported values ranging from 1.4 to 2.5 for aerosol from biomass burning, but these experiments included flaming and smoldering conditions and the samples contained EC.

The analysis results indicate that more than 97% of the aerosol mass is composed of primary organic carbon. The OC/EC analysis measured 0.3% of elemental carbon (EC) in the sample, but the filter transmission signal during the thermal optical analysis showed that this EC amount was attributed to charring of the OC and the corrected amount of EC was below the detection limit. The highest ionic mass fraction is attributed to potassium (K^+, 0.87%) followed by chloride (Cl^-, 0.74%) and sulfate (SO_4^{2-}, 0.28%). Trace amounts of nitrate (NO_3^-), ammonia (NH_4^+), carbonate (Ca^{2+}) and sodium (Na^+) were also observed in the aerosol mass. Potassium, chloride and sulfate have been previously reported as the main inorganic species in biomass burning aerosol; plume measurements by *Ferek et al.* [1998] reported mass fractions of potassium (3-5%), chloride (1-3%), and sulfate (1-3%). *Hand et al.* [2010] also reported potassium and chloride as the most abundant ions but with a high variable inorganic mass fraction depending on fuel/wood type ranging from 2% by mass (pine type woods) up to 44% by mass (for certain brush types). The findings here for oak (2.75%) fit well into the range of pine wood, but the comparison could be biased since we only measure aerosol produced by wood

pyrolysis under anoxic conditions and not from actual burning of biomass which is expected to contain more EC.

3.3.2 Organic Composition Analysis (NMR Spectroscopy Results)

Although it is desirable to understand the chemical components responsible for light absorption, traditional speciation techniques such as gas chromatography are unsuited for identifying these compounds, which probably include large and semi-polar molecules [*Sun et al.*, 2007]. *Chen and Bond* [2010] show two major differences that affect light absorption by OA. The first is the temperature of combustion: absorption per carbon increases as pyrolysis increases. The second is the nature of the extraction solvent: methanol extracts more-absorbing material than water. By comparing functional groups within these different types of OA, we can infer which components lead to absorption.

Figure 19 shows ^{1}H and ^{13}C NMR spectra for the methanol extract of OA sample generated at 425°C, a relatively high temperature. The high solvent peaks were cut off so the peaks from the sample are enlarged. Both spectra show a few sharp peaks which are attributable to major substances present at relatively high concentrations. There are many continuous small peaks, suggesting a complex mixture of substances, each occurring in low concentration.

The integrated peaks of the spectra above (Figures 20 and 21) show large contributions from C-O and aliphatic functional groups, followed by aromatic rings and C-C double bonds in the extract of the 425°C sample. Results from ^{1}H NMR indicate that there are more O-CH-O acetal functional groups in water extracts than in methanol extracts for the high-temperature spectra, which have more absorption. No significant differences are observed for other functional groups.

In ^{1}H-NMR spectroscopy, information on the chemical environment of protons is obtained, but not on the carbon structure [*Graber and Rudich*, 2006]. Therefore, alternative interpretations of ^{1}H-NMR spectra can be possible. For example, a low intensity of protons associated with aromatic carbon would indicate the abundance of hydrogen attached to aromatic carbon. This could have three causes: (1) the abundance of aromatic structure is low (2) most of the protons in the aromatic structures have been substituted and (3) there are large molecules of polycyclic aromatic compounds in which no proton is associated with aromatic carbon in the inner position. To identify the possible causes, the use of ^{13}C NMR is necessary (Figure 21).

For both high- and low-temperature samples, water extracts have less aromatic or unsaturated carbon [C=C-(C,H)], and higher content of carbon bonds with single oxygen or nitrogen (C-O or C-N). This difference was not observed in ^{1}H NMR spectra, so these unsaturated carbon bonds must be located in aromatic rings or otherwise not bonded with hydrogen. This is consistent with our hypothesis that water cannot extract large molecules with conjugated aromatic rings or C-C double bonds, and that these functional groups contribute to the more-absorbing OC in the water insoluble part.

The differing compositions of more-absorbing and less-absorbing material might affect the physical configuration of the mixed particles and the optical properties with increasing RH. At increasing RH, the water soluble components will most likely aid particle growth and these soluble components would dissolve in the added water content. The soluble OC- water mixture may remain unmixed with the strongly absorbing insoluble parts, with the combined particle being a shell-core configuration or an overall composite media. The configuration chosen affects the modeled optical properties of the mixed particle as a function of RH.

3.3.3 Evolution of OA Size Distribution in the Storage Chamber

In contrast to the benchmarking experiments, the biomass-OA was not generated continuously, because biomass combustion is inherently unstable and therefore cannot produce a stable flow. Instead, the sample aerosol is drawn from a storage vessel in which the concentration decreased with time. Because of coagulation during the long tests, the OA size distribution is a function of time. Typically the coagulation rate between particles decreases with time and the size distribution stabilizes after 15 to 20 min of residence time in the storage vessel. The changes in the dry size distribution and the changes in dry scattering were monitored with the SMPS system and a nephelometer, respectively, as described earlier. An additional effort was also made to keep the aerosol concentration in the optical instrumentation constant by increasing the flow rate through the storage chamber. The evolution of a dry OA distribution as a function of the time at which the optical measurements were taken is provided in Figure 22.

Figure 22A indicates that the peak diameter of the particle sizes is close to 300 nm and that the concentration of particles decreases with time due to dilution. In terms of distribution statistics, at t = 0 min the count median diameter (CMD) was 233 nm with a geometric standard deviation (GSD) of 1.57 while at t = 60 min the CMD was 251 nm with a GSD of 1.42. The normalized Figure 22B shows that the distribution becomes narrower with time (fraction of particles near peak diameter increased whereas other fractions decreased).

3.3.4 Hygroscopic Size Growth Factor

Figure 23 shows two independent HTDMA measurement datasets of OA generated directly from oak wood pyrolysis at 425°C. The selected dry diameter for both experiments was 200 nm which is lower than the CMD of the OA from the storage chamber. 200 nm was found to be a good compromise between sizing accuracy and scanning time for the HTDMA system. Additionally the hygroscopic size growth factor in that range was not expected to be affected significantly by the Kelvin effect and therefore the differences in hygroscopicity between 200 nm and larger dry sizes was not expected to be significant. The plotted vertical uncertainties in Figure 23 correspond to the calculated sizing uncertainty of the HTDMA system, and the horizontal error bars give the measured RH range within the humidified scanning DMA column.

Both hygroscopic growth factors f(RH)Dp from TDMAinv are very similar and their fits are almost identical, which indicates that our pyrolysis experiments are reproducible. We obtained $\kappa = 0.080 +/- 0.024$ for both experiments, which is comparable to the result of *Carrico et al.* [2008] for aerosols from combustion of sagebrush $\kappa = 0.085$ and duff core $\kappa = 0.063$ obtained from methanol extracts of filters. *Carrico et al.* [2010] obtained similar results when studying biofuel combustion aerosol generated in the smoldering phase, which have a large fraction of OC. However, they assigned a value of $\kappa = 0.03$ for OC to achieve closure between the H-TDMA derived value of κ with one reconstructed from filter speciation. *Chang et al.* [2010] studied ambient aerosols, and assumed that the hygroscopicity of OA is related to the degree of oxygenation. They obtained a $\kappa = 0.22 \pm 0.04$ for the oxygenated OA, and $\kappa = 0.15$ for the campaign-wide average hygroscopicity of OA, both higher than the $\kappa = 0.08$ reported here.

3.3.5 Optical Properties and Closure

The optical properties of humidified primary OA generated pyrolysis of oak wood are provided in Figure 24. The figure shows extinction (a), scattering (b), absorption inferred by the difference of the two (c), and the inferred single scattering albedo (d). The measured and inferred values are depicted as circles whereas the dashed and solid lines show the modeled values calculated with the Mie model. Error bars in (a) and (b) are the measured standard deviations of

σ_{ep} and σ_{sp} values for an integration time of 120 s, respectively. The error bars in (c) and (d) for the σ_{ep} and ω are calculated based on those values but only one representative error bar is shown for better clarity.

Extinction (a), scattering (b) and absorption (c) increase with increasing RH whereas the single scattering albedo (d) decreases. Dry and humidified absorption increases with decreasing wavelength, with the strongest absorption at the 467 nm wavelength and undetectable absorption at 660 nm. This wavelength dependence is similar to previous findings for biomass burning under dry conditions derived from filter measurements [*Kirchstetter et al.*, 2004] and filter extracts measured with spectrophotometry [*Y Chen and Bond*, 2010].

The determined absorption enhancements at 95% RH are 2.1 +/- 0.7 and 2.3 +/- 1.2 at the wavelengths of 467 nm and 530 nm, respectively. However, there was no detectable absorption or trend in absorption at 660 nm due to the extremely low values of absorption. It is also possible that the nature of the dry organic aerosol could change during the test, either due to coagulation or loss of semi-volatile material upon dilution. However, no significant changes in absorption were observed in tests without humidification that were otherwise identical to the experiments shown here.

The lines in Figure 21 depict closure evaluation with two different refractive index mixing rules for water and OC. The LVA rule is shown as dashed lines. This widely used model shows an overall good agreement in capturing the trend in scattering and extinction but is unable to capture the trend in the increasing absorption and decreasing SSA with RH. In contrast to LVA, the DEMA model is able to capture the trends in absorption and SSA but overall shows less accuracy in representing the absolute values, especially at 660 nm. However, the DEMA results indicate that a heterogeneously mixed aerosol with insoluble absorbing compounds can explain an absorption enhancement and lowering in single scattering albedo. In comparison to the LVA refractive index model, less accurate representation of absolute values with DEMA could be explained that the change in particle configuration is sensitive to water content and the dry refractive index of the material. The κ- model used (Figure 23) slightly over predicts the humidified aerosol sizes and therefore water content at RHs between 40 and 85% which could explain the higher modeled absorption in that range.

Most global models of organic matter optical properties do not yet account for the absorption by organic carbon emitted from biomass combustion or pyrolysis. When this absorption is represented in models, model parameterizations often assume that scattering increases but absorption remains constant as RH increases. The absorption increase with RH found in this study indicates that even parameterizations that do consider absorption measured for dry aerosol could underestimate it for RH values between 75 and 95 %. LVA or similar models are frequently used in global aerosol models. Only one model has explored the DEMA representation [*Jacobson*, 2006; 2010] and this model finds a substantial response in cloud burn-off with the increased absorption predicted by the DEMA treatment.

3.3.6 Normalized Optical Properties for Multiple Experiments

Multiple OC experiments with the same experimental conditions were performed to establish stronger confidence in the measured results. Figure 25 shows the normalized optical properties in terms of optical growth factors (Table 1) and single scattering albedo as a function of RH at 467 nm. Corresponding results at 530 and 660 nm are available in Appendix A.

Extinction and scattering results from all experiments shown in panels (a) and (b) show a similar growth pattern with increasing RH conditions and have a fairly low variability indicating

that the aerosol have similar hygroscopicity. The absorption growth factor and single scattering albedo values show overall a higher variability then the scattering and extinction values but a clear increasing trend in increasing absorption is apparent which causes the decrease in single scattering albedo with increasing RH conditions. All experiments show an increase in absorption of 2.2+/-0.7 at 95% RH in comparison to dry conditions (RH < 40%),which results in a reduction in single scattering albedo by 0.04 since the increase in scattering is less than the increase in absorption values. Similar to the results in Figure 24, the DEMA refractive index model represents the observed trends in absorption growth and single scattering albedo as a function of RH better than the LVA model indicating that changes in intra-particle configuration with RH are affecting light absorption with increasing RH.

3.4 Organic Aerosol from Wood Pyrolysis Mixed with Inorganic Solute

Three OC mixing experiments with different mass fractions of ammonium sulfate aerosol and an additional three OC mixing experiments with three different mass fractions of sodium chloride were performed. This section provides the results for these experiments in terms of composition analysis, size growth factors and optical properties.

3.4.1 Composition Analysis

Table 8 provides the composition analysis for the six mixing experiments. The three ammonium sulfate mixing experiments are named AS1 to AS3 and the three sodium chloride experiments are named NaCl1 to NaCl3. An OM/OC correction factor of 1.68 was used to convert the organic carbon to primary organic aerosol mass (for details see section 3.3.1). The densities for converting mass to volume fractions were 1.2 g/cm^3 for OM [*Cross et al.*, 2009], 1.769 g/cm^3 for ammonium sulfate and 2.165 g/cm^3 for sodium chloride [*Lide*, 2010]. A detailed table with the measured mass concentrations of all ions and OC can be found in the Appendix B.

The range of measured mass fraction of inorganic ammonium sulfate and sodium chloride to OM was fairly narrow (21%-36% by mass). The original target had been to reach distinct mass fractions between 20 and 50% by mass which was not achieved due to the difficulty of controlling the mass concentration of OC.

3.4.2 Hygroscopic Size Growth Factors

The measured size growth factors of each ammonium sulfate and sodium chloride mixing experiment are shown in Figure 26. The dry selected diameter was 200 nm. Panel (a) provides results for the ammonium sulfate mixtures and panel (b) provides results for the sodium chloride mixtures at the three mass fractions of inorganic solute. Blue green and red colors indicate the different solute mass fractions.

Even with small amounts of inorganic solute (21% - 26% by mass), a deliquescent behavior of the mixtures is visible, but the deliquescence is less distinct than for the pure inorganic solute (indicated as dashed black line) and the deliquescence (79.5% RH for ammonium sulfate and 76% RH for sodium chloride) is shifted towards a lower RH. Shifts in deliquescence of internal organic/ inorganic aerosol mixtures have been observed previously [*Andrews and Larson*, 1993; *Hansson et al.*, 1998]. The size growth factors of ammonium sulfate show no distinguishable trend with the three different inorganic solute mass fractions tested here. However, for the sodium chloride mixtures a clear distinguishable trend is observable with increased growth factors with higher inorganic mass fractions. The exact reason why no trend is distinguishable in the ammonium sulfate data is not clear but could be attributed to the large

uncertainties in the determined inorganic mass fraction with ion chromatography and OC/EC analysis, and/or the lower degree hygroscopicity for AS compared to NaCl.

3.4.3 Optical Properties

The following two sections contain the optical closure analysis for the OC/AS and OC/NaCl mixtures. The results are reported for 467 nm normalized as optical growth factors. Results for non-normalized closure results are provided in Appendix C. The DEMA model is used to model the refractive index of the results (Section 2.10.1)

Ammonium Sulfate Mixtures

The optical properties at the 467 nm wavelength of humidified primary OA generated by oak wood pyrolysis mixed with ammonium sulfate are provided in Figure 27. The figure shows the extinction growth factor (a), scattering growth factor (b), absorption growth factor inferred by the difference of the two (c), and the inferred single scattering albedo (d) as a function of increasing RH conditions. The measured and inferred values are depicted as symbols for which each color and symbol shape representing a different mass fraction of AS to OM. The solid lines show the modeled values calculated with the DEMA-Mie model using a fixed 28% mass fraction of ammonium sulfate which is the "medium" mass fraction determined by filter analysis. Only one mass fraction was used for the modeled results since the HTDMA measurements (section 3.4.2) did not show any significant difference between the measured growth factors for the three samples.

Extinction and scattering growth factors (panels a and b) show no change until the deliquescence RH where they start to increase rapidly. Similar to the size growth factor results shown in Figure 26a, there is no distinguishable difference in optical growth factors between the different mass fractions of ammonium sulfate. However, there is a difference in single scattering albedo (d) which could be explained by slight differences in the generation of the aerosol (pyrolysis process) and dry size. Even though the modeling for these results used the same ammonium sulfate mass fraction of 28% there is a slight difference in the modeled results for the three experiments which is explained by the variability of the dry size distribution at each RH. This also causes the somewhat noisy appearance of the modeled results. Overall, light absorption increases above the deliquescence RH reaching an increase by a factor of 2 at 95% RH, which is in the same range of the pure OC results shown in Figure 22c. Refractive index results from DEMA allow good descriptions of all optical properties including the increase in light absorption after deliquescence.

Sodium Chloride Mixtures

The optical properties at 467 nm of humidified primary OA generated by oak wood pyrolysis mixed with NaCl are shown in Figure 28. The figure shows the extinction growth factor (a), scattering growth factor (b), absorption growth factor inferred by the difference of the two (c), and the inferred single scattering albedo (d) as a function of increasing RH conditions. The measured and inferred values are depicted as colored symbols for which each color and symbol shape representing a different mass fraction of sodium chloride. The solid lines show the modeled values calculated with the Mie model for each mass fraction of sodium chloride.

The extinction and scattering growth factors (panels a and b) show no change until the deliquescence RH where they start to increase rapidly. There is distinguishable difference in optical growth factors between the 21 and 25 % mass fractions of sodium chloride, but the

results for the 25 and 30% mass fraction look almost identical, which is contradictory to size growth factor results shown in Figure 26b. The slight difference in single scattering albedo (d) can be explained by the different mass fraction of ammonium sulfate; the lowest mass fraction corresponds to the lowest single scattering albedo. The modeled results for the 21 and 25% mass fraction agree well with the measurements for scattering and extinction growth. For light absorption and single scattering albedo the measurements are noisy but the model represents the trends with RH. Overall, light absorption increases above the deliquescence RH and such increases are similar to the ammonium sulfate mixtures and pure OC results. The DEMA model is able to capture the increasing trends.

4 SUMMARY AND CONCLUSIONS

Light extinction and light scattering by aerosol at high relative humidities were measured in the laboratory to determine light absorption by difference. This project successfully developed instrumentation that provided measurements of light absorption, scattering, extinction and single scattering albedo between 32 and 95% RH. Benchmarks of the system were accomplished with humidified ammonium sulfate, absorbing polystyrene microspheres, and nigrosin. The difference method was capable of measuring single scattering albedo of absorbing polystyrene microspheres within 0.02 of previously reported results. Light absorption of the nigrosin benchmark was enhanced by a factor of 1.24 +/- 0.06 at 95% RH compared to 38% RH. To the best of our knowledge, this is the first instrumentation capable of measuring extinction, scattering, and absorption simultaneously as a function of RH up to 95%.

Absorption by atmospherically relevant OC aerosols generated from wood pyrolysis increased by a factor of 2.1 +/- 0.7 and 2.3 +/- 1.2 between 32 and 95% RH at the wavelengths of 467 nm and 530 nm respectively. This increase in absorption has not been measured previously.

Several mixing models, including the common linear-volume approximation and core-shell models, were not able to predict the increase in absorption. Only the dynamic effective medium approximation (DEMA) model was able to capture the increasing absorption trend with RH, consistent with the notion of a heterogeneous internal mixture with insoluble absorbing components. This model predicts greater absorption than assumed in common atmospheric models.

NMR analysis found a greater fraction of molecules with conjugated aromatic rings or C-C double bonds in the more-absorbing, water-insoluble fraction. Therefore, there are differences in chemical composition that affect both solubility and absorption, as well as the physical configuration of the mixed particles.

Mixing the biomass OC aerosol with select mass fractions of ammonium sulfate ranging from 25 to 36% and sodium chloride ranging from 21 to 30% resulted in an increase in light scattering and extinction with RH and inorganic mass fraction. However, the current results showed that the increase in light absorption behavior was similar to that of pure biomass OC for the same growth factor. The DEMA was furthermore able to capture the trends for the optical properties for both mixing experiments above the deliquescence RH.

This research provides focused laboratory studies that are directly relevant to determining optical properties by aerosols for use in global transport and climate models. Many global models of organic matter optical properties do not yet account for the absorption by organic carbon emitted from biomass combustion or pyrolysis. The findings presented here indicate that even parameterizations that do consider absorption measured for dry aerosol could underestimate it for RH values between 75 and 95 %. Because these particles also serve as cloud condensation nuclei, absorption within cloud droplets may also be underrepresented.

5 TABLES

Table 1. Overview of measurements and derived properties

Measured Properties			
Property	**Description**	**Equipment**	**Comment**
σ_{ep}	Extinction Coefficient	Short Path Extinction Cell (SPEC)	λ = 467, 530, 660 nm < 98.5% RH
σ_{sp}	Scattering Coefficient	Two TSI 3563 Nephelometer[1]	λ = 470, 530, 660 nm[1] λ = 450, 550, 700 nm
D_p	Particle Size Distribution	TSI 3936 SMPS	(dry)
RH	Relative Humidity	Two Vaisala HMP 233, Four Sensirion SHT	Sensirion SHT in HTDMA
T	Temperature	Four Thermocouple, Two Vaisala HMP 233, Four Sensirion SHT	Sensirion SHT in HTDMA
T_{DP}	Dew-point Temperature	Three General Eastern M1	One in HTDMA
$f(RH)D_p$	Size Growth Factor	HTDMA	D_p(dry) = 100 or 200 nm
Derived Properties			
σ_{ap}	Absorption Coefficient	Difference of σ_{ep} and σ_{sp}	λ = 467, 530, 660 nm
ω	Single Scattering Albedo	Quotient of σ_{ap} and σ_{ep}	λ = 467, 530, 660 nm
$f(RH)\sigma_{ep}$	σ_{ep} Growth Factor	Quotient of σ_{ep}(RH) and σ_{ep}(dry RH)	Dry typically below 8% RH otherwise stated
$f(RH)\sigma_{sp}$	σ_{sp} Growth Factor	Quotient of σ_{sp}(RH) and σ_{sp}(dry RH)	Dry typically below 8% RH otherwise stated
$f(RH)\sigma_{ap}$	σ_{ap} Growth Factor	Quotient of σ_{ap}(RH) and σ_{ap}(dry RH)	Dry typically below 8% RH otherwise stated
κ	Hygroscopicity Parameter	From HTDMA Data Analysis	
Offline Measurements from Collected Aerosol Filter Mass			
c (OC/ EC)	Organic- and Elemental Carbon Concentration	Sunset Laboratory OC/EC Analyzer	Quartz Filter
c (ions)	Ion Concentrations	Various (see 2.8.2)	Nylon Filter
Functional groups	Nuclear Magnetic Resonance (NMR) Spectroscopy	Varian Unity 500 ^{1}H and ^{13}C NMR	Filter Extracts

1. Two nephelometers were used but one instrument was modified to the wavelengths of 470, 530 and 660 nm for a better comparison with the SPEC; additionally the lamp heating of this instrument was reduced to less than 0.5°C for a better performance at high RH. Details can be found in section 2.4.2.

Table 2 Aerosol types, aerosol generation method and purpose for tests

Aerosol Type	Generation Method	Purpose
Ammonium sulfate $(NH_4)_2SO_4$ poly-disperse	Atomizer (TSI 3076)	"White" benchmark for dry and humidified conditions
Dyed polystyrene microspheres diameter = 327 nm	Atomizer (TSI 3076)	Absorbing benchmark for dry conditions
Nigrosin ($C_{48}N_9H_{51}$) poly-disperse	Atomizer (TSI 3076)	Absorbing benchmark for dry and humidified conditions
Organic (from wood pyrolysis) poly-disperse	Temperature controlled pyrolysis reactor	Light absorption of OA under dry and humidified conditions
Organic mixed with $(NH_4)_2SO_4$ poly-disperse	Pyrolysis reactor and Atomizer	Light absorption of OA mixture under dry and humidified conditions
Organic mixed with NaCl poly-disperse	Pyrolysis reactor and Atomizer	Light absorption of OA mixture under dry and humidified conditions

Table 3 Categorized functional groups in ^{1}H-NMR

Range (ppm_m)	Functional Groups
0.6-1.8	Aliphatic hydrogen (R-*H)*
1.8-3.1	Hydrogen in α position to carbonyl or aromatic carbon (=C-C-*H*)
3.1-4.4	Protons attached to carbon atoms singly bonded to oxygen (*H*-C-O)
4.4-5.5	Hemiacetals and acetals (O-C *H*-O)
6.0-7.0	Vinylic hydrogen (=C-*H*)
6.5-8.4	Aromatic hydrogen (Ar-*H)*
9.0-12.0	Carbonxylic acids (OH) and aldehydes (O=C *H*- or *H*O-C=O)
Solvent Residual Signals	
2.48-2.52	DMSO
3.10-3.25	Methanol as CH_3
4.00-4.02	Methanol as *OH*
3.30-3.34	H_2O

Table 4 Categorized functional groups in ^{13}C-NMR.

Range (ppm_m)	Functional Groups
0-45	Alkyl (*C*-*C*)
45-95	*N*-alkyl (*C*-N) or *O*-alkyl (*C*-O)
95-110	Anomeric / acetal *C* (O-*C*-O)
110-140	Aromatic and unsaturated *C* (C=*C*-(C,H))
140-160	Aromatic *C* bonded to N or O (C=*C*-(O,N))
160-190	Carboxylic acids / ester, amide (O=*C*-(OH/NH_2))
190-230	Carbonyl C of aldehydes and ketones (O=*C*-(R, H))
Solvent Residual Signals	
Range (ppm_m)	**Functional groups**
39-41	DMSO
49-49.5	Methanol

Table 5 Linear regression coefficients obtained for a regression between the measured scattering and measured extinction for dry ammonium sulfate to obtain correction factors for non-idealities in the extinction cell. All R^2 values were greater than 0.99 and the regression equation was $\sigma_{ep,\,corrected} = \sigma_{sp} = Intercept + Slope \times \sigma_{ep,\,measured}$.

	λ = 467 nm		λ = 530 nm		λ = 660 nm	
	Slope	Intercept	Slope	Intercept	Slope	Intercept
$\sigma_{ep,\,corrected}$ (Mm^{-1})	0.987 +/- 0.011	-4.989 +/- 24.116	1.012 +/- 0.011	- 6.176 +/- 22.034	1.031 +/- 0.0481	- 14.886 +/- 21.396

Table 6: Linear regression coefficients from comparison between the modeled and measured scattering ($\sigma_{sp,\,model} = Intercept + Slope \times \sigma_{sp,\,measured}$) of dry ammonium sulfate. All R^2 values were greater than 0.99.

	λ = 467 nm		λ = 530 nm		λ = 660 nm	
	Slope	Intercept	Slope	Intercept	Slope	Intercept
$\sigma_{sp,\,model}$ (Mm^{-1})	0.985 +/- 0.012	-10.664 +/- 23.793	1.027 +/- 0.016	-12.831 +/- 22.295	1.061 +/- 0.078	-22.310 +/- 30.876

Table 7 Composition analysis of OC aerosol generated by the pyrolysis of oak wood at 425°C. Elemental carbon (EC) and the ions Br^-, PO_4^{3-} and Mg^{2+} were also determined but the results were below the detection limit of the analysis

	OM*	OM/OC	Cl^-	$SO4^{2-}$	NO^{3-}	NH^{4+}	Ca^{2+}	K^+	Na^+
Mean	97.25	1.68	0.74	0.28	0.21	0.07	0.21	0.87	0.17
Std. Deviation	1.13	0.09	0.23	0.04	0.20	0.08	0.15	0.25	0.06

*Corrected by forcing closure with gravimetric mass (OM/OC describes the correction factor)

Table 8 Composition analysis results for the six mixing experiments in terms of mass and volume fraction of the inorganic solutes ammonium sulfate $(NH_4)_2SO_4$ and sodium chloride (NaCl) to OM.

Sample	$(NH_4)_2SO_4$ (% m)	$(NH_4)_2SO_4$ (% v)	NaCl (% m)	NaCl (% v)
AS 1	**36.0**	**27.9**	0.2	0.2
AS 2	**28.2**	**21.4**	1.7	1
AS 3	**25.9**	**19.7**	4.3	2.7
NaCl 1	1.2	0.9	**25.1**	**16.0**
NaCl 2	1.4	1.1	**30.3**	**20.2**
NaCl 3	0.3	0.2	**20.5**	**12.6**

6 FIGURES

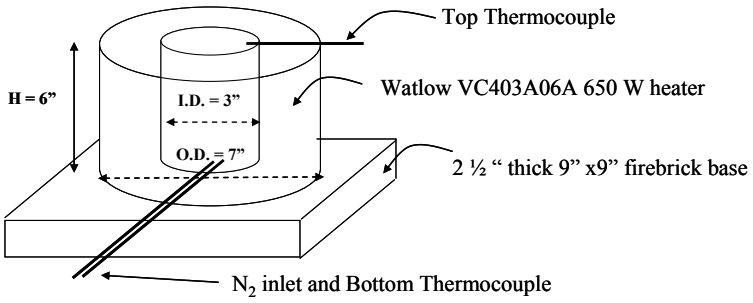

Figure 1 Temperature controlled wood pyrolysis reactor for the generation of OA

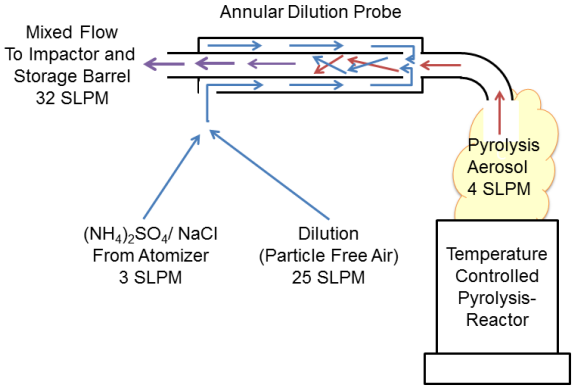

Figure 2 Mixing of Pyrolysis OA with Ammonium Sulfate and Sodium Chloride

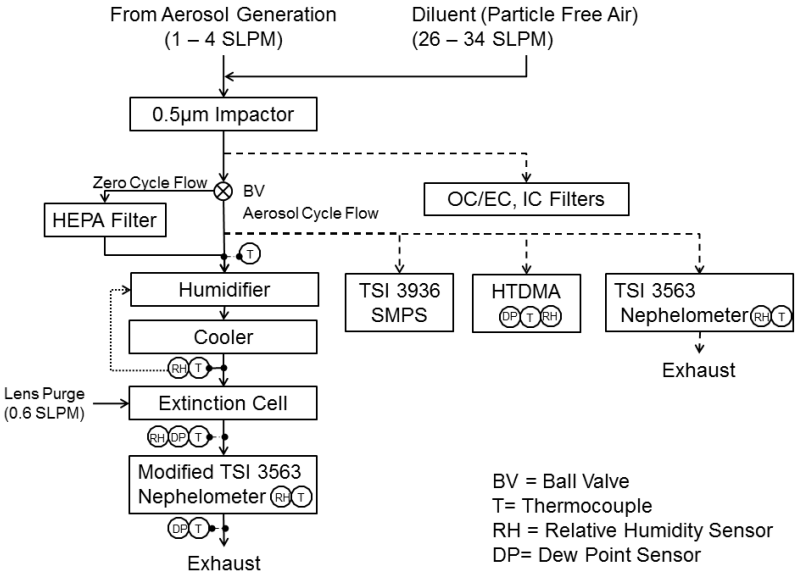

Figure 3 Instrumentation Assembly

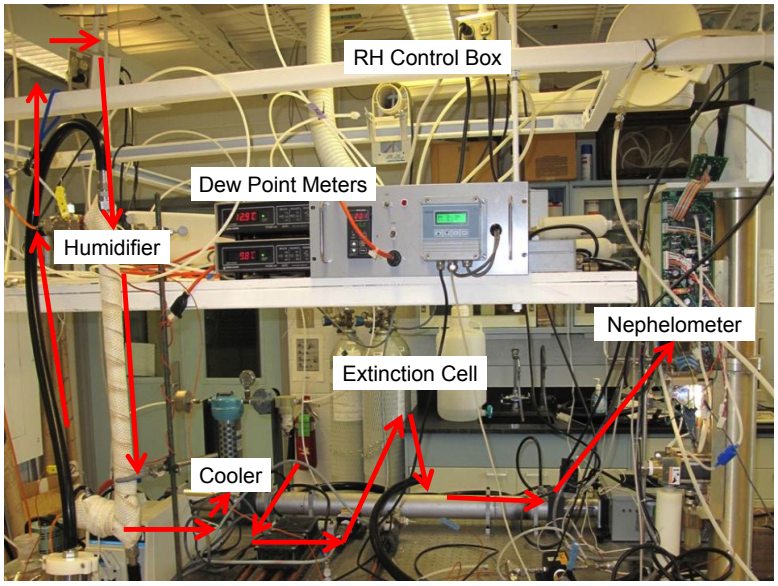

Figure 4 Photograph of instrument assembly

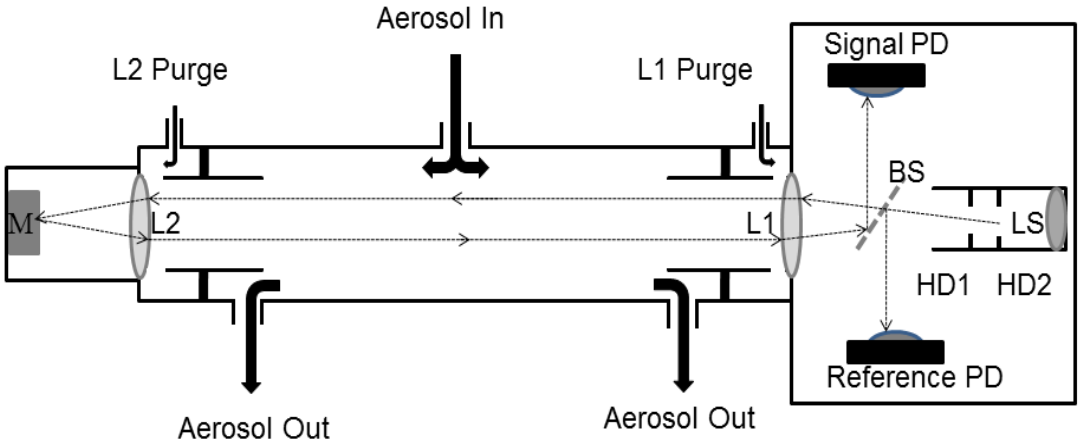

Figure 5 Short Path Extinction Cell (SPEC) overview; M is a silver plated mirror, L1 and L2 are achromatic lenses, BS is a beam splitter, PD are photo detectors, HD1 and HD2 are holographic diffusers, and LS is the light source.

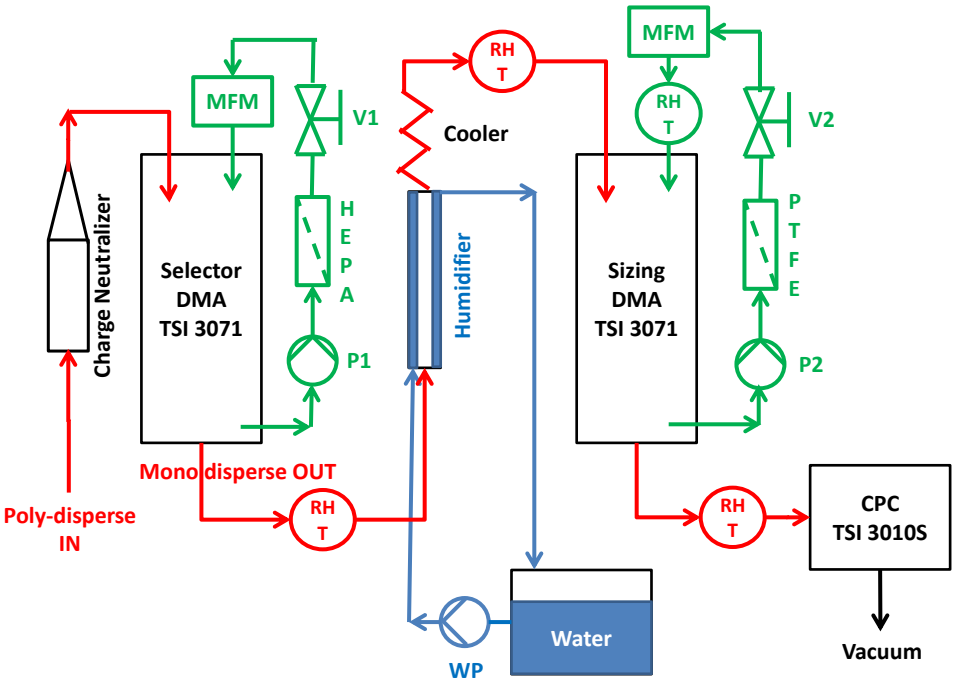

Figure 6 HTDMA system overview: red = aerosol flow, green = sheath air flow, blue = liquid water flow for the humidifier, WP = water pump, P1, P2 = sheath air pumps and V1, V2 = needle valves.

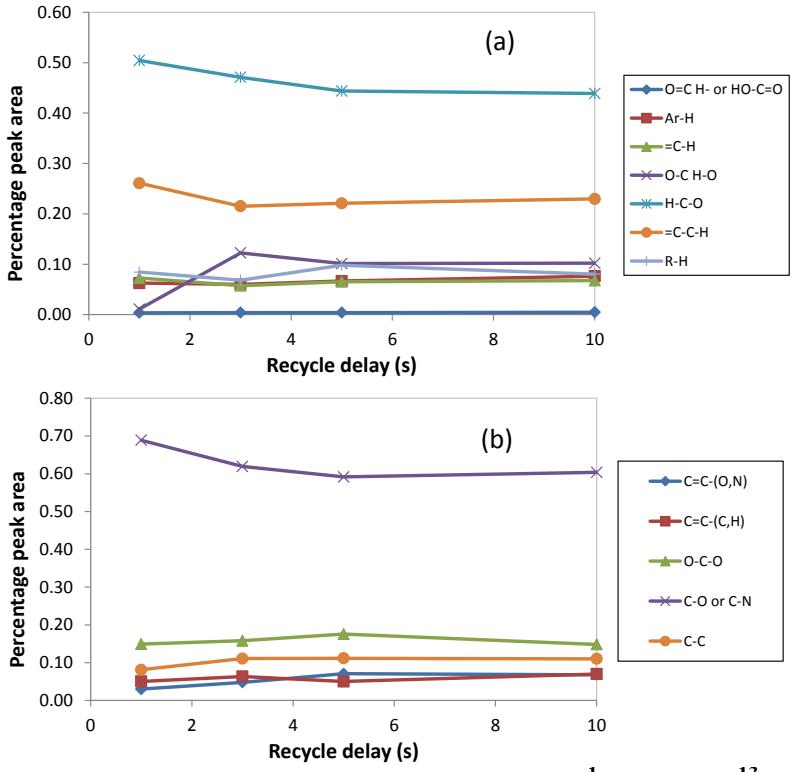

Figure 7 Determination of the recycle delay for (a) ^{1}H and (b) ^{13}C NMR

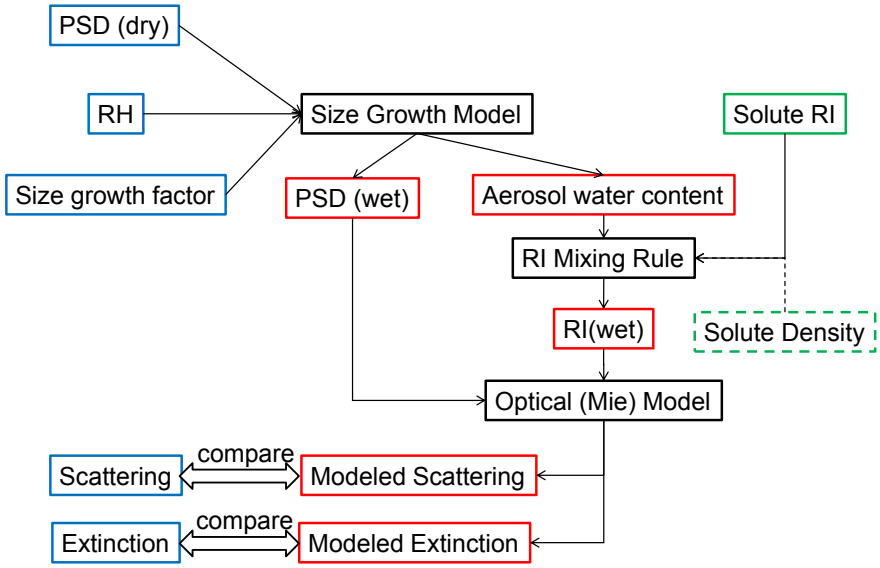

Figure 8 Optical modeling and closure evaluation approach; blue = measured variables, green = model parameters, black = model and red = modeled variables. PSD = Particle size distribution. RI = Refractive index

Figure 9 Conceptual overview of the LVA a) and DEMA b) refractive index mixing rules

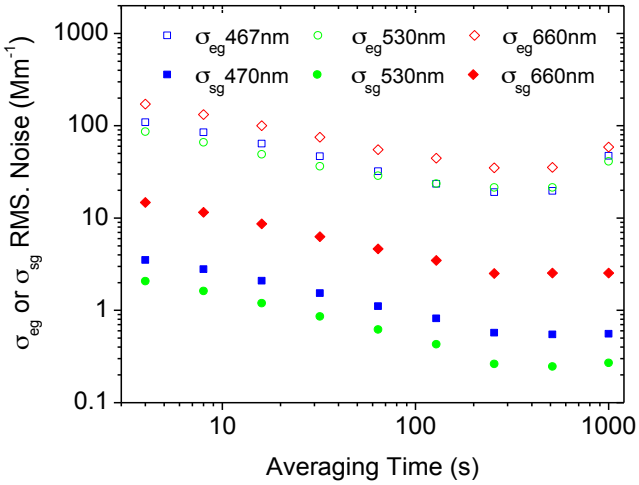

Figure 10 Root mean square (RMS) noise values for particle free air extinction and scattering as a function of wavelength and sample averaging time for the extinction cell and the modified nephelometer, respectively

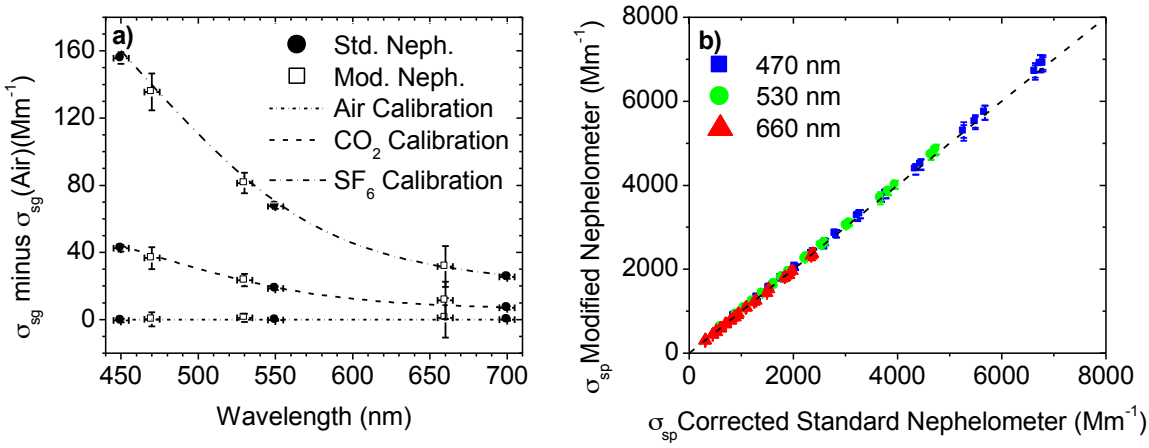

Figure 11 Evaluation of the optical modified and temperature controlled nephelometer. a) Measured Rayleigh scattering values for the calibration gases air (Zero), CO_2 (Span1) and SF_6 (Span2) for standard TSI 3563 nephelometer (circles) and modified TSI 3563 (squares). Dashed lines indicate theoretical values b) Comparison of scattering values from the modified nephelometer and the wavelength interpolated unmodified nephelometer determined with ammonium sulfate aerosol at different aerosol concentrations. The dashed line indicates ideal correlation. For all three wavelengths, the instruments differ less than 1.5%.

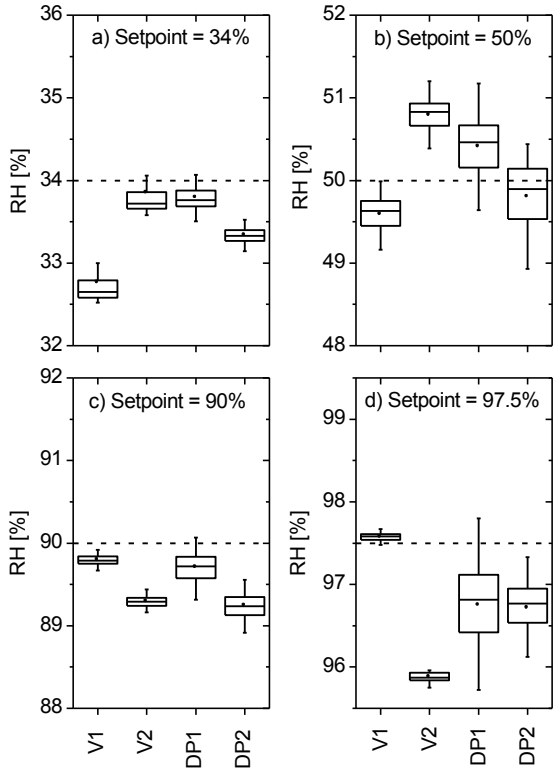

Figure 12 RH sensor agreement at RH set point values of: a) 34% RH, b) 50% RH, c) 90% and d) 97.5%. V1 and V2 are the capacitive-based RH values. DP1 and DP2 are the dew point-based RH values calculated with co-located dry-bulb temperature measurements.

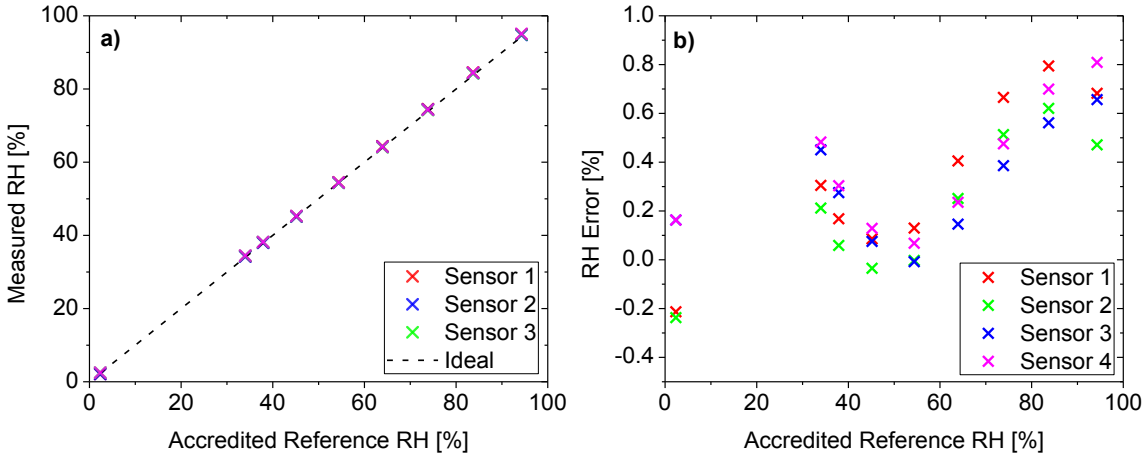

Figure 13 Performance of HTDMA RH sensors after sensor calibration in relation to the reference RH measured by sensors calibrated according to NIST. Panel a) comparison of absolute values with the ideal correlation indicated by the line, b) Residuals.

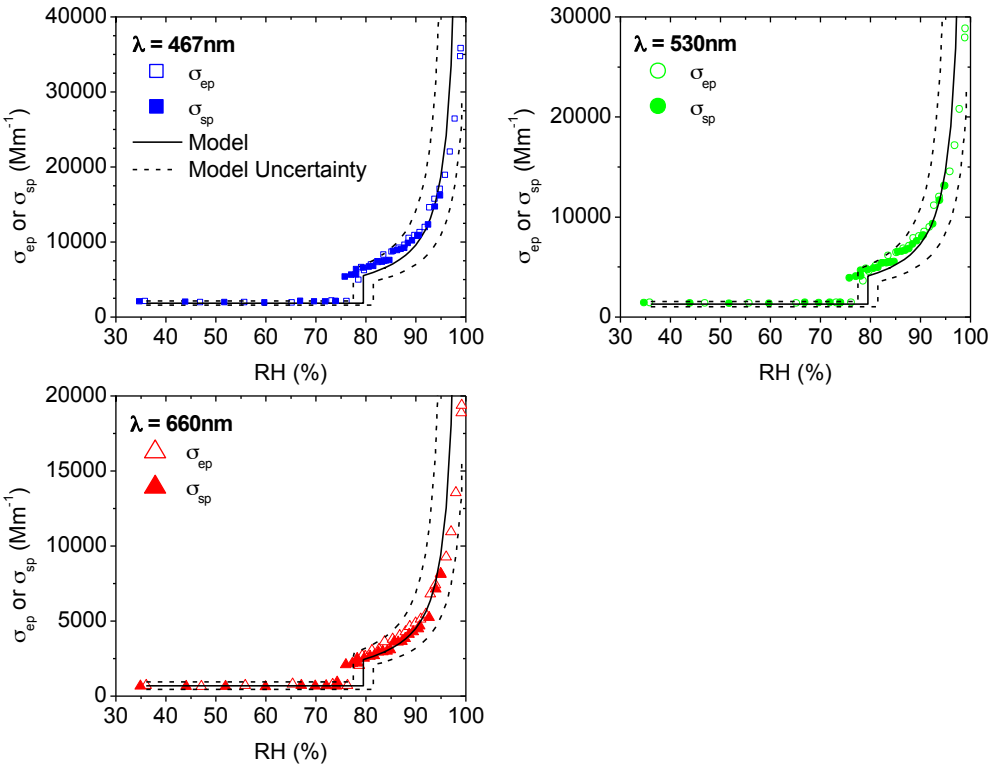

Figure 14 Measured σ_{sp} and σ_{ep} coefficients for ammonium sulfate aerosol as a function of RH. Experimental values are presented as symbols. Modeled values and their uncertainties are indicated as solid and dashed lines, respectively.

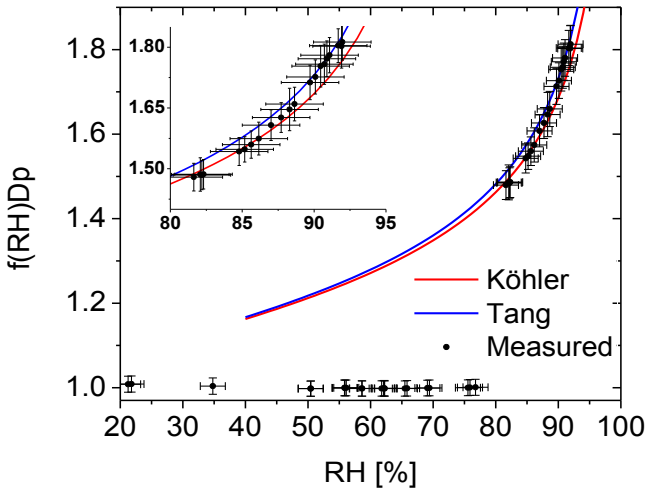

Figure 15 Evaluation of HTDMA performance with ammonium sulfate particles with a dry diameter of 100 nm.

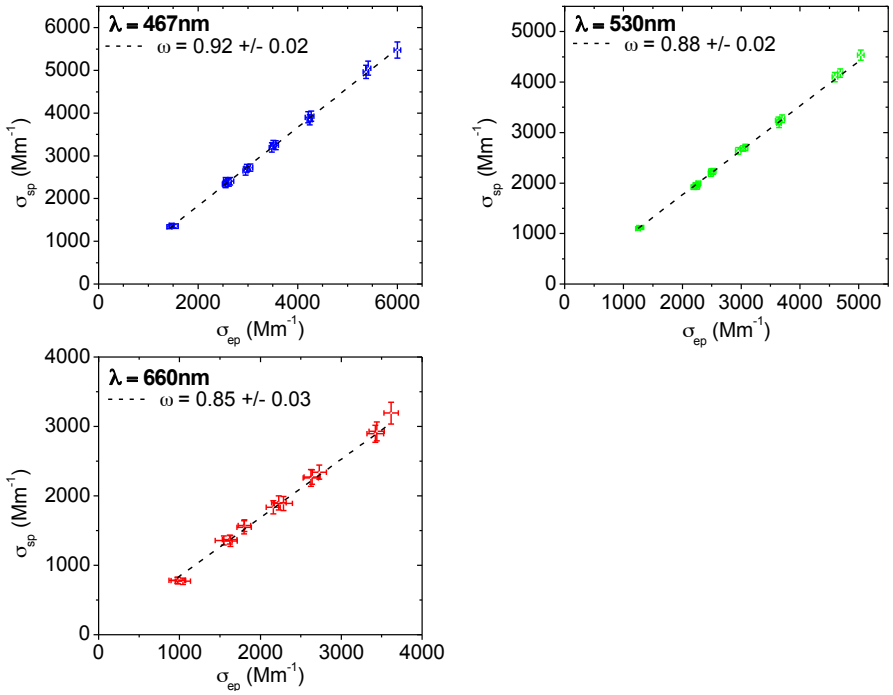

Figure 16 Dependence of measured scattering (σ_{sp}) vs. extinction (σ_{ep}) coefficients at three wavelengths (symbols) on concentration of 327 nm diameter light absorbing PSL microspheres. A linear best fit (dashed line) was used to determine the single scattering albedo ω

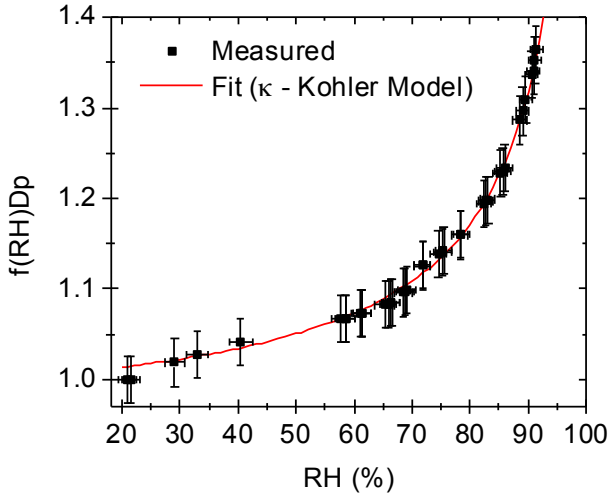

Figure 17 Nigrosin HTDMA measurement results for the determination of the hygroscopicity parameter κ. Selected dry particle size was 100 nm

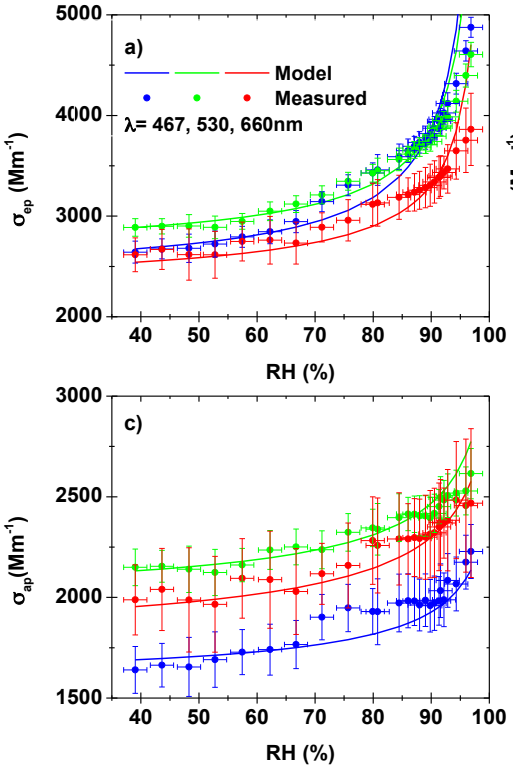

d)

RH	f(RH)σ_{ap}, (λ= 530 nm)		ω (λ= 530 nm)	
	Measured	Modeled	Measured	Modeled
85%	1.11 +/- 0.07	1.11	0.33 +/- 0.02	0.32
90%	1.14 +/- 0.06	1.16	0.36 +/- 0.02	0.36
95%	1.22 +/- 0.06	1.27	0.42 +/- 0.03	0.44

Figure 18 Measured and modeled optical properties of nigrosin as a function of RH. Extinction and scattering for 467 nm, 530 nm and 660 nm are shown in panels a and b, calculated absorption by difference in extinction and scattering is shown in panel c. d shows the obtained absorption growth factor and single scattering albedo values in comparison to the model at 530 nm

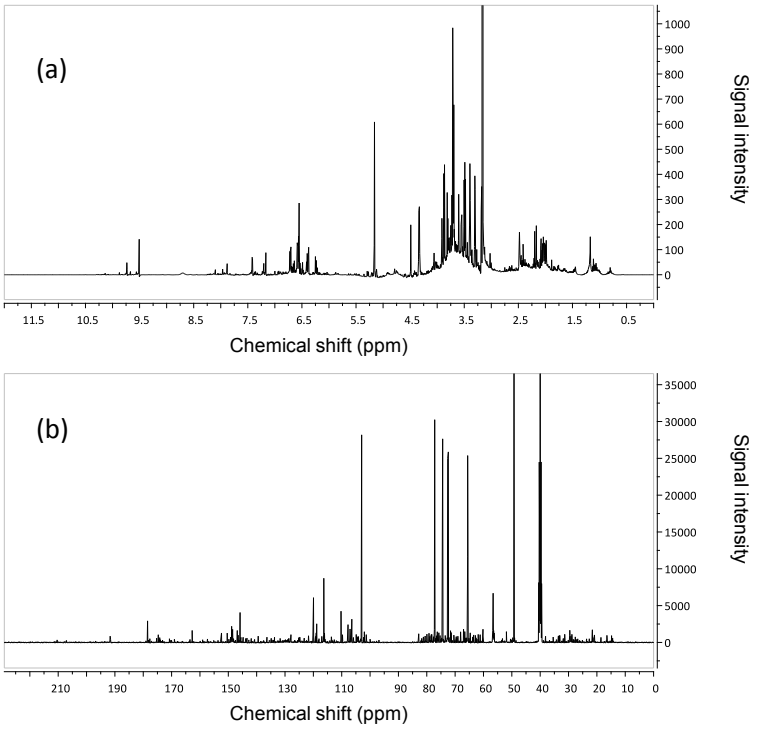

Figure 19 NMR spectra of methanol extract of sample at 425°C a) ^{1}H and b) ^{13}C. The reported chemical shifts are relative to the solvent. The chemical shifts of the solvent (DMSO-d_6) are identified according to *Fulmer et al.* [2010].

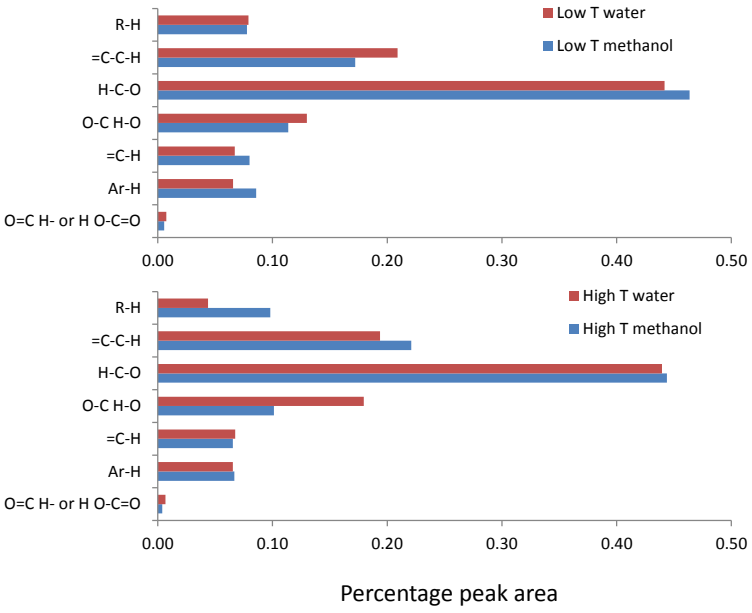

Figure 20 Percentage of total ^{1}H NMR peak area under each spectral region for methanol and water extracts of OC generated at low (300°C) and high (425°C) temperatures

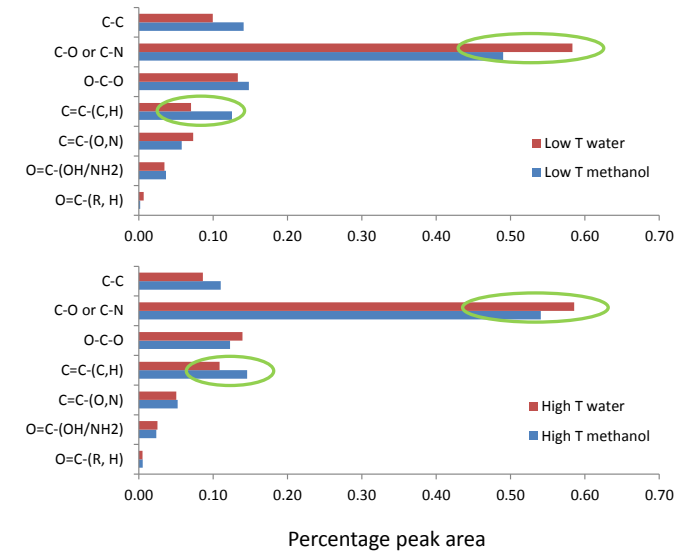

Figure 21 Percentage of total ^{13}C NMR peak area under each spectral region for methanol and water extracts of OC generated at two temperatures. Difference of contribution from two major functional groups is highlighted with green circles. "Low T" and "High T" correspond to 300 and 425°C respectively

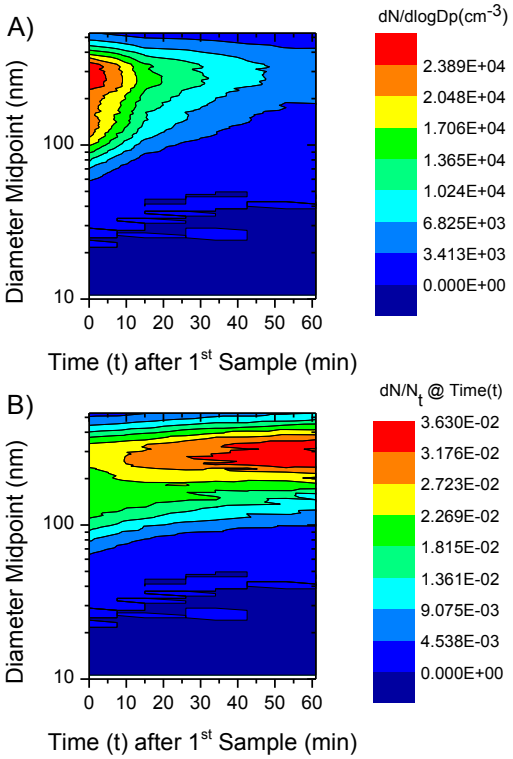

Figure 22 Evolution of the dry pyrolysis OA size distribution during the optical measurement. A) Normalized by SMPS bin width, B) Normalized by total number of particles N_t present at time t

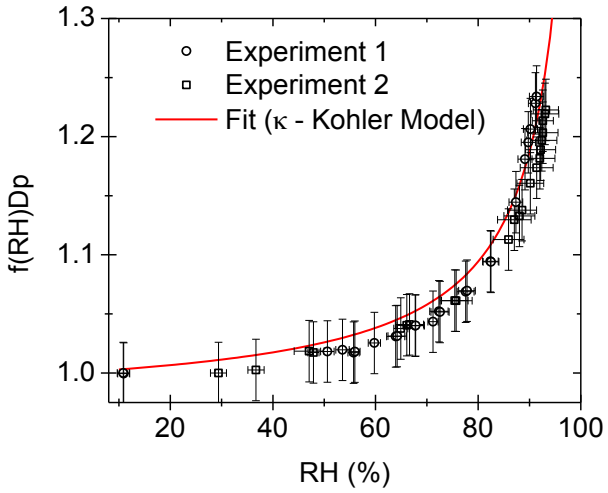

Figure 23 HTDMA measurement results of OA to determine the hygroscopicity parameter, κ. Selected dry particle size was 200 nm. Experiment 1 & 2 are two independent datasets from independent wood pyrolysis events

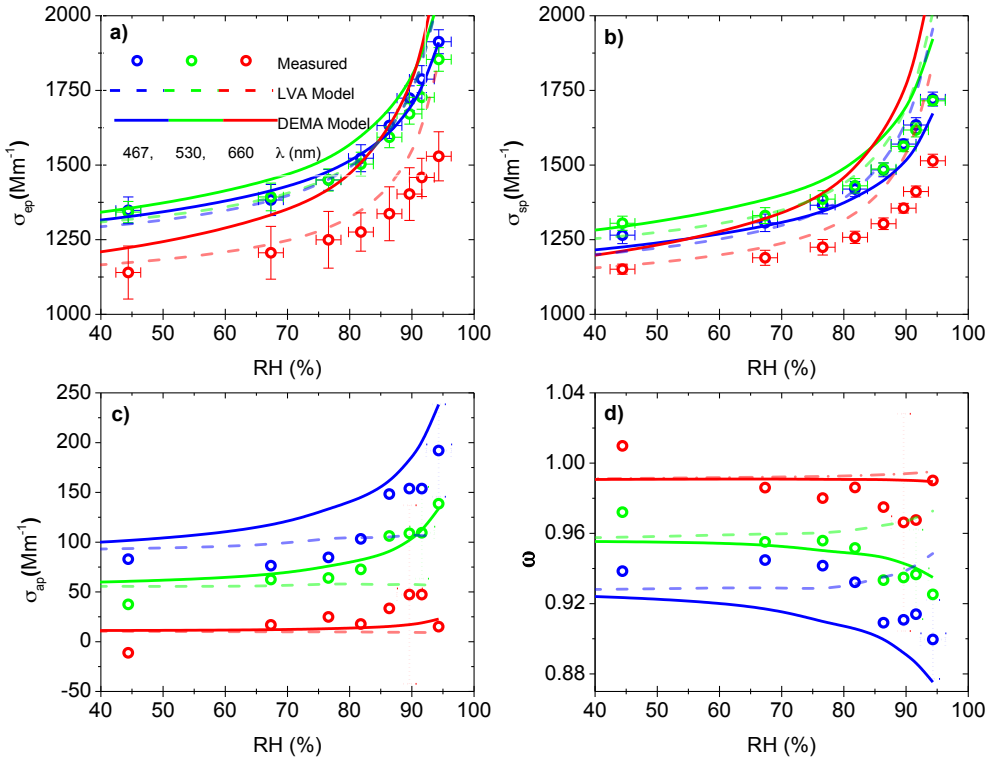

Figure 24 Measured and modeled optical properties of biomass OC aerosol as a function of RH. Circles correspond to the measured values. The dashed lines are the modeled results using the linear volume average (LVA) refractive index mixing rule. Solid lines correspond to the dynamic effective medium approximation (DEMA) refractive index model.

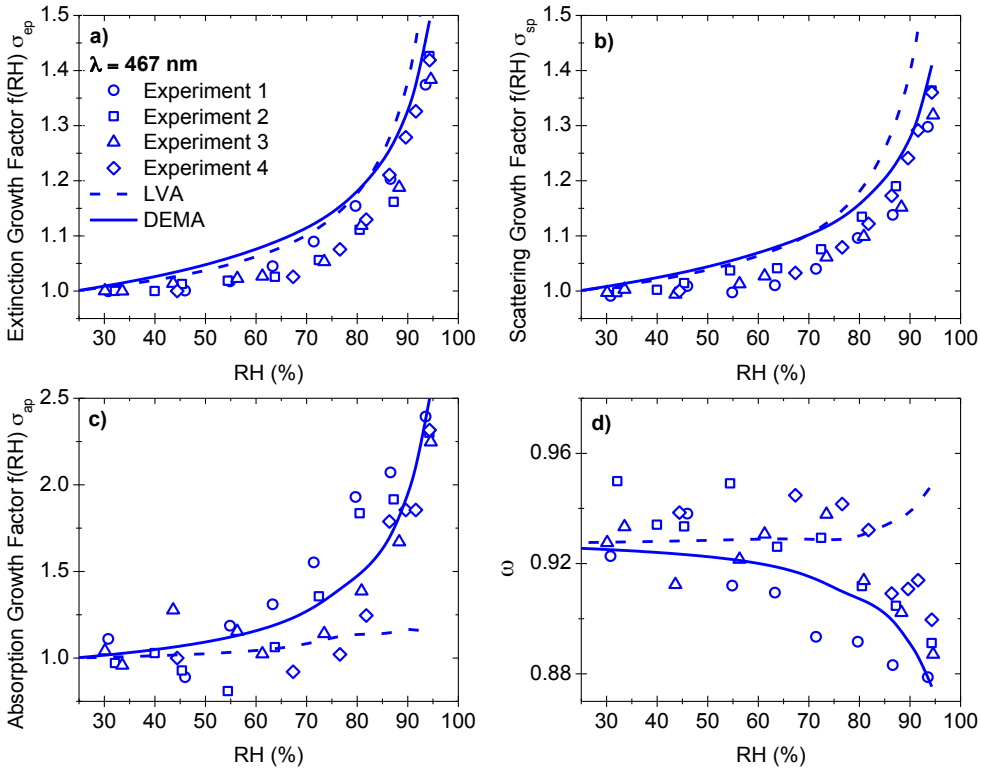

Figure 25 Normalized optical properties at 467 nm for four OC experiments generated at the same pyrolysis reactor conditions (425°C) Symbols depict measured values for different experiments whereas the lines correspond to the LVA (dashed) and DEMA (solid) modeled values.

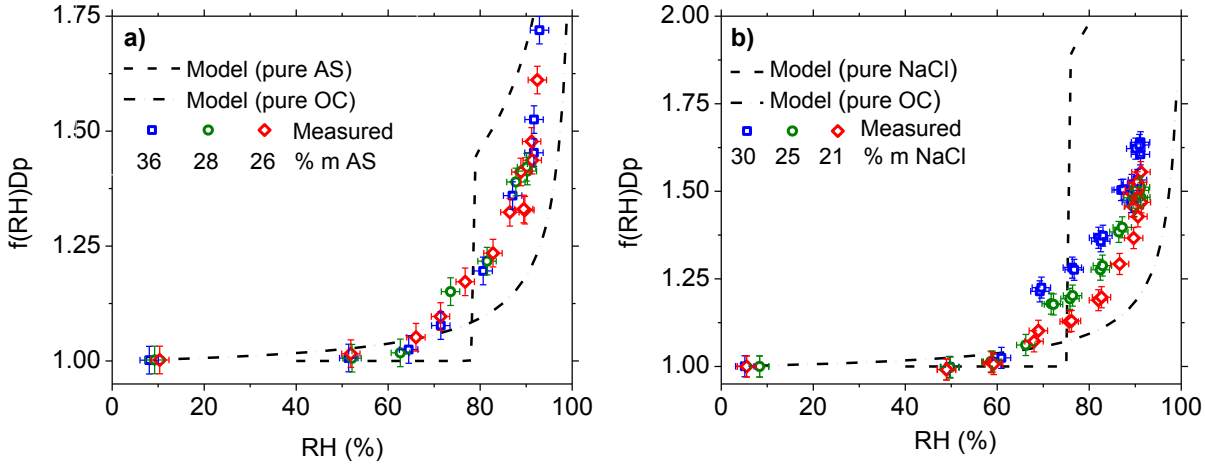

Figure 26 Measured and modeled diameter growth factors as a function of RH for OC particles mixed with ammonium sulfate (a) and OC particles mixed with sodium chloride (b) at three inorganic solute mass fractions. The dry selected diameter was 200 nm. The black dashed lines show the modeled growth factors for pure inorganic solute and pure pyrolysis OC, respectively.

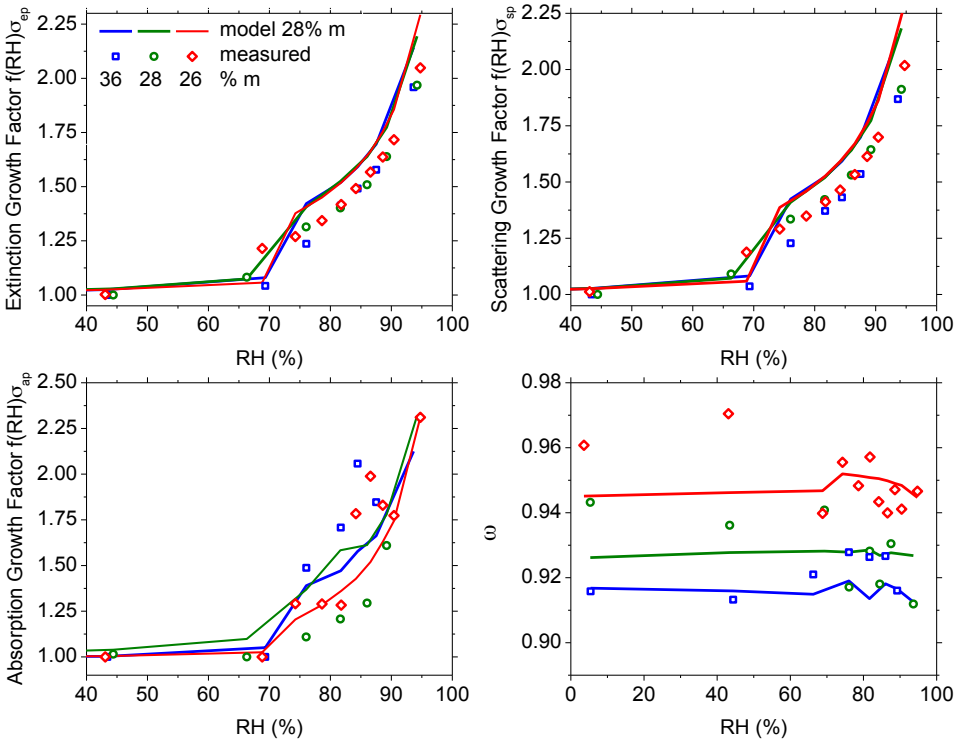

Figure 27 Optical growth factors and single scattering albedo at the 467nm wavelength for the pyrolysis OC mixtures with three different mass fractions of ammonium sulfate.

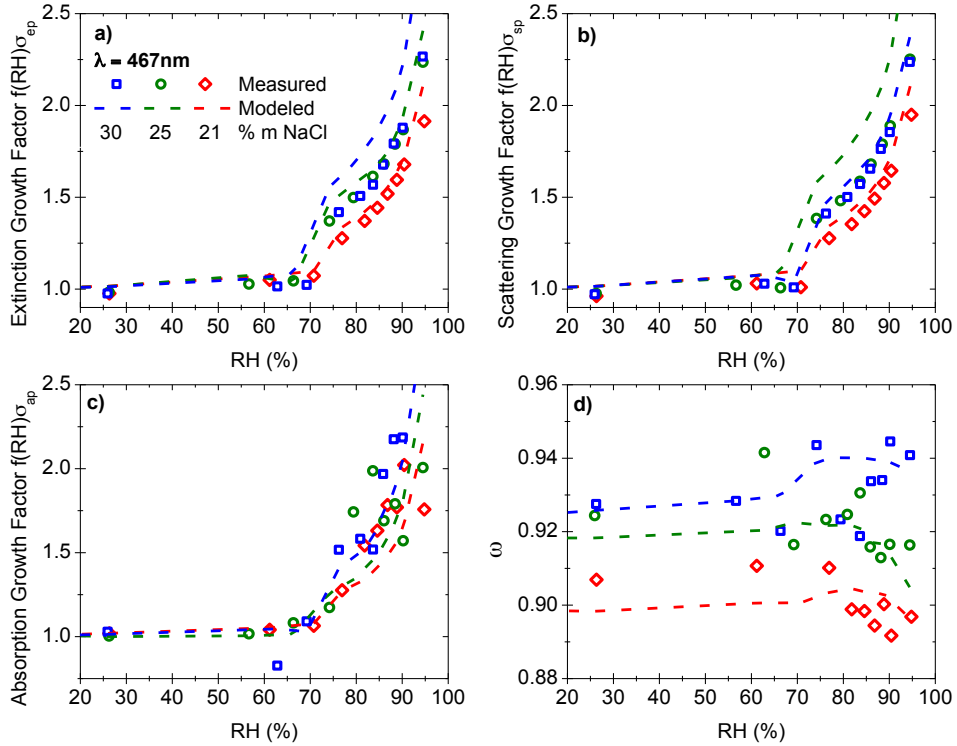

Figure 28 Optical growth factors and single scattering albedo at the 467nm wavelength for the pyrolysis OC mixtures with three different mass fractions of NaCl

7 PUBLICATIONS

Peer Reviewed Publications

Brem, B., Mena, F., Rood, M.J., Bond, T.C. (2011) Measured Optical Properties of Inorganic and Organic Aerosols at Relative Humidities up to 95%. *Aerosol Science and Technology,* 46 (2). 178 - 190.

Peer Reviewed Manuscripts in Preparation/ Submitted

Mena, F., Brem, B**.**, Rood, M.J., Bond, T.C. (2012) Optical Closure Analysis of Absorbing Organic Aerosols at Relative Humidities up to 95%. *In Preparation for ACP*.

Brem, B., Mena, F., Torres, A., Rood, M.J., Bond, T.C. (2012) Optical Properties of Organic Inorganic Pyrolyis Aerorsol Mixtures at Relative Humidities up to 95%. *In Preparation*.

8 PRESENTATIONS

Brem, B., Mena, F.,Chen, Y., Rood, M.J., Bond, T.C. (2012) Optical Properties of Moderately Absorbing Organic and Mixed Organic/inorganic Particles at High Humidities, *3rd Science Team Meeting of the DOE Atmospheric System Research (ASR) Program*, Crystal City, VA, Platform Presentation.

Brem, B., Mena, F.,Chen, Y., Rood, M.J., Bond, T.C. (2011) Measurement of Optical Properties of Organic and Mixed Organic/ Inorganic Laboratory Aerosols at Relative Humidities between 8 and 95%, *AAAR's 30th Annual Conference*, Orlando, FL, Platform Presentation, No. 3A1.

Brem, B., Rood, M.J., Bond, T.C. (2011) Optical Properties of Moderately-Absorbing Organic and Mixed Organic/Inorganic Particles at Very High Humidities, *2nd Science Team Meeting of the DOE Atmospheric System Research (ASR) Program,* San Antonio, TX, Poster.

Brem, B., Mena, F., Rood, M.J., Bond, T.C. (2010) Methods to Reduce Sample Heating of a TSI 3563 Nephelometer when Measuring Light Scattering Coefficients at High Relative Humidities *A&WMA's 103rd Annual Meeting & Exhibition*, Calgary, AB., No. 1155.

Brem, B., Rood, M.J., Bond, T.C. (2010) Optical Properties of Moderately-Absorbing Organic and Mixed Organic/Inorganic Particles at Very High Humidities, *1st Science Team Meeting of the DOE Atmospheric System Research (ASR) Program,* Bethesda, MD, Poster.

Brem, B., Mena, F., Rood, M.J., Bond, T.C. (2009) Performance Evaluation of a Short Path Extinction Cell at High Relative Humidities, *Fall Meeting of the American Geophysical Union,* San Francisco, CA, Poster.

Brem, B**.**, Mena, F., Rood, M.J., Bond, T.C. (2009) Development and Performance Evaluation of a Short Path Extinction Cell (SPEC), *A&WMA's 102nd Annual Meeting & Exhibition*, Detroit, MI., No. 318,

9 REFERENCES

Anderson, T. L., and J. A. Ogren (1998), Determining aerosol radiative properties using the TSI 3563 integrating nephelometer, *Aerosol Sci Tech*, *29*(1), 57-69.

Anderson, T. L., et al. (1996), Performance characteristics of a high-sensitivity, three-wavelength, total scatter/backscatter nephelometer, *Journal of Atmospheric and Oceanic Technology*, *13*(5), 967-986.

Andrews, E., and S. M. Larson (1993), Effect of Surfactant Layers on the Size Changes of Aerosol-Particles as a Function of Relative-Humidity, *Environ Sci Technol*, *27*(5), 857-865.

Arnott, W. P., H. Moosmuller, P. J. Sheridan, J. A. Ogren, R. Raspet, W. V. Slaton, J. L. Hand, S. M. Kreidenweis, and J. L. Collett (2003), Photoacoustic and filter-based ambient aerosol light absorption measurements: Instrument comparisons and the role of relative humidity, *Journal of Geophysical Research-Atmospheres*, *108*(D1).

Aspnes, D. E. (1982), Optical Properties of Thin-Films, *Thin Solid Films*, *89*(3), 249-262.

Berner, A., C. Lurzer, F. Pohl, O. Preining, and P. Wagner (1979), Size distribution of the urban aerosol in Vienna, *Sci Total Environ*, *13*(3), 245-261.

Bodhaine, B. A. (1979), Measurement of the Rayleigh-scattering properties of some gases with a nephelometer, *Appl Optics*, *18*(1), 121-125.

Bohren, C. E., and D. R. Huffman (1983), *Absorption and Scattering of Light by Small Particles*, Wiley and Sons.

Bond, T. C. (2001), Spectral dependence of visible light absorption by carbonaceous particles emitted from coal combustion, *Geophys Res Lett*, *28*(21), 4075-4078.

Bond, T. C., T. L. Anderson, and D. Campbell (1999), Calibration and intercomparison of filter-based measurements of visible light absorption by aerosols, *Aerosol Sci Tech*, *30*(6), 582-600.

Bond, T. C., G. Habib, and R. W. Bergstrom (2006), Limitations in the enhancement of visible light absorption due to mixing state, *Journal of Geophysical Research-Atmospheres*, *111*(D20), -
.

Bond, T. C., D. S. Covert, and T. Muller (2009), Truncation and Angular-Scattering Corrections for Absorbing Aerosol in the TSI 3563 Nephelometer, *Aerosol Sci Tech*, *43*(9), 866-871.

Boucher, O., and T. L. Anderson (1995), General circulation model assessment of the sensitivity of direct climate forcing by anthropogenic sulfate aerosols to aerosol size and chemistry, *Journal of Geophysical Research-Atmospheres*, *100*(D12), 26117-26134.

Carrico, C. M., M. J. Rood, and J. A. Ogren (1998), Aerosol light scattering properties at Cape Grim, Tasmania, during the First Aerosol Characterization Experiment (ACE 1), *Journal of Geophysical Research-Atmospheres*, *103*(D13), 16565-16574.

Carrico, C. M., M. J. Rood, J. A. Ogren, C. Neususs, A. Wiedensohler, and J. Heintzenberg (2000), Aerosol optical properties at Sagres, Portugal during ACE-2, *Tellus Series B-Chemical and Physical Meteorology*, *52*(2), 694-715.

Carrico, C. M., M. D. Petters, S. M. Kreidenweis, J. L. Collett, G. Engling, and W. C. Malm (2008), Aerosol hygroscopicity and cloud droplet activation of extracts of filters from biomass burning experiments, *Journal of Geophysical Research-Atmospheres*, *113*(D8).

Carrico, C. M., M. D. Petters, S. M. Kreidenweis, A. P. Sullivan, G. R. McMeeking, E. J. T. Levin, G. Engling, W. C. Malm, and J. L. Collett (2010), Water uptake and chemical composition of fresh aerosols generated in open burning of biomass, *Atmos Chem Phys*, *10*(11), 5165-5178.

Chang, R. Y. W., J. G. Slowik, N. C. Shantz, A. Vlasenko, J. Liggio, S. J. Sjostedt, W. R. Leaitch, and J. P. D. Abbatt (2010), The hygroscopicity parameter (kappa) of ambient organic aerosol at a field site subject to biogenic and anthropogenic influences: relationship to degree of aerosol oxidation, *Atmos Chem Phys*, *10*(11), 5047-5064.

Chen, Y., and T. C. Bond (2010), Light absorption by organic carbon from wood combustion, *Atmos Chem Phys*, *10*(4), 1773-1787.

Chen, Z., and C. Lu (2005), Humidity sensors: A review of materials and mechanisms, *Sens. Lett.*, *3*(4), 274-295.

Chylek, P., and V. Srivastava (1983), Dielectric-Constant of a Composite Inhomogenous-Medium, *Phys Rev B*, *27*(8), 5098-5106.

Covert, D. S., R. J. Charlson, and N. C. Ahlquist (1970), Study of relationship of chemical composition and humidity with light scattering by aerosols, *Bull. Amer. Meteorol. Soc.*, *51*(10), 1010-&.

Cross, E. S., T. B. Onasch, M. Canagaratna, J. T. Jayne, J. Kimmel, X. Y. Yu, M. L. Alexander, D. R. Worsnop, and P. Davidovits (2009), Single particle characterization using a light scattering module coupled to a time-of-flight aerosol mass spectrometer, *Atmos Chem Phys*, *9*(20), 7769-7793.

Duarte, R. M. B. O., E. B. H. Santos, C. A. Pio, and A. C. Duarte (2007), Comparison of structural features of water-soluble organic matter from atmospheric aerosols with those of aquatic humic substances, *Atmos Environ*, *41*(37), 8100-8113.

Ferek, R. J., J. S. Reid, P. V. Hobbs, D. R. Blake, and C. Liousse (1998), Emission factors of hydrocarbons, halocarbons, trace gases and particles from biomass burning in Brazil, *Journal of Geophysical Research-Atmospheres*, *103*(D24), 32107-32118.

Fulmer, G. R., A. J. M. Miller, N. H. Sherden, H. E. Gottlieb, A. Nudelman, B. M. Stoltz, J. E. Bercaw, and K. I. Goldberg (2010), NMR Chemical Shifts of Trace Impurities: Common Laboratory Solvents, Organics, and Gases in Deuterated Solvents Relevant to the Organometallic Chemist, *Organometallics*, *29*(9), 2176-2179.

Garvey, D. M., and R. G. Pinnick (1983), Response Characteristics of the Particle Measuring System Active Scattering Aerosol Spectromenter Probe (ASASP-X), *Aerosol Sci Tech*, *2*(4), 477-488.

Gates, R. S. (1994), Dew-point temperature error from measuring dry-bulb temperature and relative-humidity, *Transactions of the Asae*, *37*(2), 687-688.

Ghan, S. J., and R. A. Zaveri (2007), Parameterization of optical properties for hydrated internally mixed aerosol, *Journal of Geophysical Research-Atmospheres*, *112*(D10), 10.

Graber, E. R., and Y. Rudich (2006), Atmospheric HULIS: How humic-like are they? A comprehensive and critical review, *Atmos Chem Phys*, *6*, 729-753.

Graham, B., O. L. Mayol-Bracero, P. Guyon, G. C. Roberts, S. Decesari, M. C. Facchini, P. Artaxo, W. Maenhaut, P. Koll, and M. O. Andreae (2002), Water-soluble organic compounds in biomass burning aerosols over Amazonia - 1. Characterization by NMR and GC-MS, *Journal of Geophysical Research-Atmospheres*, *107*(D20), -.

Gysel, M., G. B. McFiggans, and H. Coe (2009), Inversion of tandem differential mobility analyser (TDMA) measurements, *J Aerosol Sci*, *40*(2), 134-151.

Hand, J. L., D. E. Day, G. M. McMeeking, E. J. T. Levin, C. M. Carrico, S. M. Kreidenweis, W. C. Malm, A. Laskin, and Y. Desyaterik (2010), Measured and modeled humidification factors of fresh smoke particles from biomass burning: role of inorganic constituents, *Atmos Chem Phys*, *10*(13), 6179-6194.

Hansson, H. C., M. J. Rood, S. Koloutsou-Vakakis, K. Hameri, D. Orsini, and A. Wiedensohler (1998), NaCl aerosol particle hygroscopicity dependence on mixing with organic compounds, *J Atmos Chem*, *31*(3), 321-346.

Haywood, J. M., V. Ramaswamy, and L. J. Donner (1997), A limited-area-model case study of the effects of sub-grid scale variations in relative humidity and cloud upon the direct radiative forcing of sulfate aerosol, *Geophys Res Lett*, *24*(2), 143-146.

Heintzenberg, J., and G. Erfurt (2000), Modification of a commercial integrating nephelometer for outdoor measurements, *J. Atmos. Ocean. Technol.*, *17*(12), 1645-1650.

Jacobson, M. Z. (1999), Isolating nitrated and aromatic aerosols and nitrated aromatic gases as sources of ultraviolet light absorption, *Journal of Geophysical Research-Atmospheres*, *104*(D3), 3527-3542.

Jacobson, M. Z. (2000), A physically-based treatment of elemental carbon optics: Implications for global direct forcing of aerosols, *Geophys Res Lett*, *27*(2), 217-220.

Jacobson, M. Z. (2006), Effects of externally-through-internally-mixed soot inclusions within clouds and precipitation on global climate, *J Phys Chem A*, *110*(21), 6860-6873.

Jacobson, M. Z. (2010), Short-term effects of controlling fossil-fuel soot, biofuel soot and gases, and methane on climate, Arctic ice, and air pollution health, *Journal of Geophysical Research-Atmospheres*, *115*.

Khalizov, A. F., H. X. Xue, L. Wang, J. Zheng, and R. Y. Zhang (2009), Enhanced Light Absorption and Scattering by Carbon Soot Aerosol Internally Mixed with Sulfuric Acid, *J Phys Chem A*, *113*(6), 1066-1074.

Kirchstetter, T. W., T. Novakov, and P. V. Hobbs (2004), Evidence that the spectral dependence of light absorption by aerosols is affected by organic carbon, *Journal of Geophysical Research-Atmospheres*, *109*(D21), 12.

Koloutsou-Vakakis, S., C. M. Carrico, P. Kus, M. J. Rood, Z. Li, R. Shrestha, J. A. Ogren, J. C. Chow, and J. G. Watson (2001), Aerosol properties at a midlatitude Northern Hemisphere continental site, *Journal of Geophysical Research-Atmospheres*, *106*(D3), 3019-3032.

Kus, P., C. M. Carrico, M. J. Rood, and A. Williams (2004), Measured and modeled light scattering values for dry and hydrated laboratory aerosols, *J. Atmos. Ocean. Technol.*, *21*(7), 981-994.

Lack, D. A., E. R. Lovejoy, T. Baynard, A. Pettersson, and A. R. Ravishankara (2006), Aerosol absorption measurement using photoacoustic spectroscopy: Sensitivity, calibration, and uncertainty developments, *Aerosol Sci Tech*, *40*(9), 697-708.

Lack, D. A., C. D. Cappa, E. S. Cross, P. Massoli, A. T. Ahern, P. Davidovits, and T. B. Onasch (2009a), Absorption Enhancement of Coated Absorbing Aerosols: Validation of the Photo-Acoustic Technique for Measuring the Enhancement, *Aerosol Sci Tech*, *43*(10), 1006-1012.

Lack, D. A., et al. (2009b), Relative humidity dependence of light absorption by mineral dust after long-range atmospheric transport from the Sahara, *Geophys Res Lett*, *36*, 5.

Lang-Yona, M., Y. Rudich, E. Segre, E. Dinar, and A. Abo-Riziq (2009), Complex Refractive Indices of Aerosols Retrieved by Continuous Wave-Cavity Ring Down Aerosol Spectrometer, *Anal. Chem.*, *81*(5), 1762-1769.

Lewis, K. A., et al. (2009), Reduction in biomass burning aerosol light absorption upon humidification: roles of inorganically-induced hygroscopicity, particle collapse, and photoacoustic heat and mass transfer, *Atmos Chem Phys*, *9*(22), 8949-8966.

Lide, D. R. (Ed.) (2010), *CRC Handbook of Chemistry and Physics*, 91 ed., 2610 pp., Taylor & Francis Group, New York.

Liu, Y. G., and P. H. Daum (2008), Relationship of refractive index to mass density and self-consistency of mixing rules for multicomponent mixtures like ambient aerosols, *J Aerosol Sci*, *39*(11), 974-986.

McMurry, P. H., and M. R. Stolzenburg (1989), On the Sensitivity of Particle-Size to Relative-Humidity for Los-Angeles Aerosols, *Atmos Environ*, *23*(2), 497-507.

Mehra, R. (2003), Application of refractive index mixing rules in binary systems of hexadecane and heptadecane with n-alkanols at different temperatures, *Proc. Indian Acad. Sci.-Chem. Sci.*, *115*(2), 147-154.

Mikhailov, E., S. Vlasenko, S. T. Martin, T. Koop, and U. Poschl (2009), Amorphous and crystalline aerosol particles interacting with water vapor: conceptual framework and experimental evidence for restructuring, phase transitions and kinetic limitations, *Atmos Chem Phys*, *9*(24), 9491-9522.

Mikhailov, E. F., S. S. Vlasenko, I. A. Podgorny, V. Ramanathan, and C. E. Corrigan (2006), Optical properties of soot-water drop agglomerates: An experimental study, *Journal of Geophysical Research-Atmospheres*, *111*(D7), -.

Murphy, D. M. (2009), The Effect of Water Evaporation on Photoacoustic Signals in Transition and Molecular Flow, *Aerosol Sci Tech*, *43*(4), 356-363.

NIOSH (2003), Manual of Analytical Methods 5040, Issue 3, edited, National Institute for Occupational Safety and Health.

Orr Jr, C., F. K. Hurd, and W. J. Corbett (1958), Aerosol size and relative humidity, *Journal of Colloid Science*, *13*(5), 472-482.

Petters, M. D., and S. M. Kreidenweis (2007), A single parameter representation of hygroscopic growth and cloud condensation nucleus activity, *Atmos Chem Phys*, *7*(8), 1961-1971.

Postigo, M., S. Canzonieri, and A. Mariano (2008), Refractive and volumetric properties for binary liquid mixtures containing toluene and linear esters at 298.15 K, *J. Mol. Liq.*, *143*(2-3), 115-118.

Rader, D. J., and P. H. McMurry (1986), Application of the Tandem Differential Mobility Analyzer to Studies of Droplet Growth or Evaporation, *J Aerosol Sci*, *17*(5), 771-787.

Ramaswamy, V., and J. T. Kiehl (1985), Sensitivities of the radiative forcing due to large loadings of smoke and dust aerosols, *Journal of Geophysical Research-Atmospheres*, *90*(ND3), 5597-5613.

Reid, J. S., P. V. Hobbs, C. Liousse, J. V. Martins, R. E. Weiss, and T. F. Eck (1998), Comparisons of techniques for measuring shortwave absorption and black carbon content of aerosols from biomass burning in Brazil, *Journal of Geophysical Research-Atmospheres*, *103*(D24), 32031-32040.

Rose, D., S. S. Gunthe, E. Mikhailov, G. P. Frank, U. Dusek, M. O. Andreae, and U. Poschl (2008), Calibration and measurement uncertainties of a continuous-flow cloud condensation nuclei counter (DMT-CCNC): CCN activation of ammonium sulfate and sodium chloride aerosol particles in theory and experiment, *Atmos Chem Phys*, *8*(5), 1153-1179.

Sannigrahi, P., A. P. Sullivan, R. J. Weber, and E. D. Ingall (2006), Characterization of water-soluble organic carbon in urban atmospheric aerosols using solid-state C-13 NMR spectroscopy, *Environ Sci Technol*, *40*(3), 666-672.

Sedlacek, A., and J. Lee (2006), Direct Aerosol Absorption Measurements using Photothermal Interferometry, paper presented at U.S. DOE ASP Science Team Meeting.

Sedlacek, A., and J. Lee (2007), Photothermal interferometric aerosol absorption spectrometry, *Aerosol Sci Tech*, *41*(12), 1089-1101.

Subramanian, R., C. A. Roden, P. Boparai, and T. C. Bond (2007), Yellow beads and missing particles: Trouble ahead for filter-based absorption measurements, *Aerosol Sci Tech*, *41*(6), 630-637.

Sun, H. L., L. Biedermann, and T. C. Bond (2007), Color of brown carbon: A model for ultraviolet and visible light absorption by organic carbon aerosol, *Geophys Res Lett*, *34*(17), 5.

Swietlicki, E., et al. (2008), Hygroscopic properties of submicrometer atmospheric aerosol particles measured with H-TDMA instruments in various environments - a review, *Tellus B*, *60*(3), 432-469.

Tagliavini, E., F. Moretti, S. Decesari, M. C. Facchini, S. Fuzzi, and W. Maenhaut (2006), Functional group analysis by HNMR/chemical derivatization for the characterization of organic aerosol from the SMOCC field campaign, *Atmos Chem Phys*, *6*, 1003-1019.

Tang, I. N. (1996), Chemical and size effects of hygroscopic aerosols on light scattering coefficients, *Journal of Geophysical Research-Atmospheres*, *101*(D14), 19245-19250.

Tang, I. N., and H. R. Munkelwitz (1994), Water activities, densities, and refractive-indexes of aqueous sulfates and sodium-nitrate droplets of atmospheric importance, *Journal of Geophysical Research-Atmospheres*, *99*(D9), 18801-18808.

Virkkula, A., N. C. Ahlquist, D. S. Covert, P. J. Sheridan, W. P. Arnott, and J. A. Ogren (2005), A three-wavelength optical extinction cell for measuring aerosol light extinction and its application to determining light absorption coefficient, *Aerosol Sci Tech*, *39*(1), 52-67.

Watson, J. G. (2002), Visibility: Science and regulation, *J. Air Waste Manage. Assoc.*, *52*(6), 628-713.

Weingartner, E., H. Saathoff, M. Schnaiter, N. Streit, B. Bitnar, and U. Baltensperger (2003), Absorption of light by soot particles: determination of the absorption coefficient by means of aethalometers, *Journal of Aerosol Science*, *34*(10), 1445-1463.

Weiss, R. E. (1992), Optical extinction properties of smoke from the Kuwait oil fires, *Journal of Geophysical Research-Atmospheres*, *97*(D13), 14537-14540.

WMO (2008), WMO Guide to Meteorological Instruments and Methods of Observation, edited.

Zhang, R. Y., A. F. Khalizov, J. Pagels, D. Zhang, H. X. Xue, and P. H. McMurry (2008), Variability in morphology, hygroscopicity, and optical properties of soot aerosols during atmospheric processing, *P Natl Acad Sci USA*, *105*(30), 10291-10296.

Zieger, P., R. Fierz-Schmidhauser, M. Gysel, J. Strom, S. Henne, K. E. Yttri, U. Baltensperger, and E. Weingartner (2010), Effects of relative humidity on aerosol light scattering in the Arctic, *Atmos Chem Phys*, *10*(8), 3875-3890.

APPENDIX A

Normalized optical properties at 530 nm for 4 OC experiments generated at the same conditions (425°C) Symbols depict different experiments whereas the line correspond to the LVA (dashed) and DEMA (solid) models

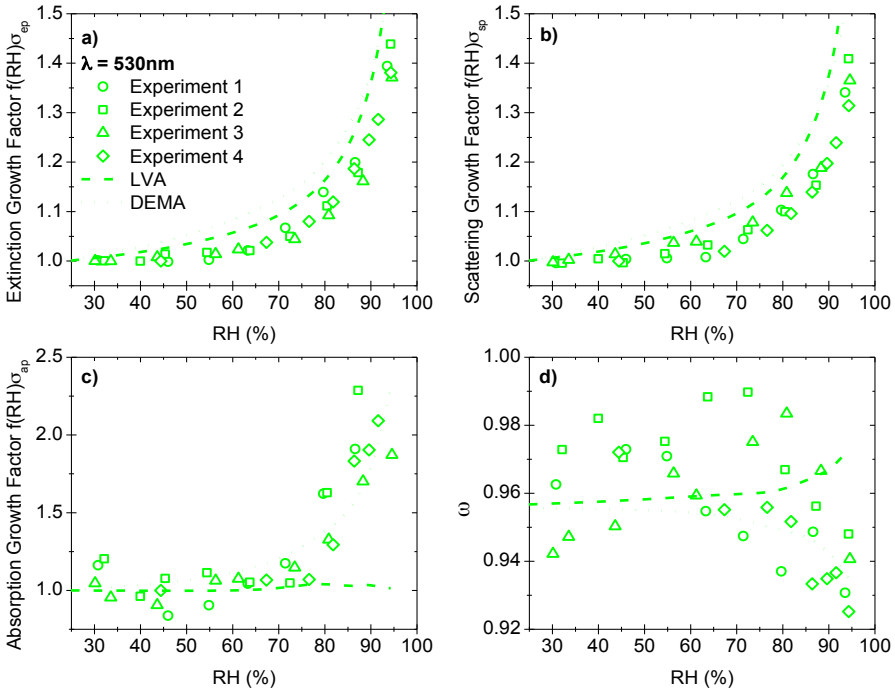

Normalized optical properties at 660 nm for 4 OC experiments generated at the same conditions (425°C) Symbols depict different experiments whereas the line correspond to the LVA (dashed) and DEMA (solid) models

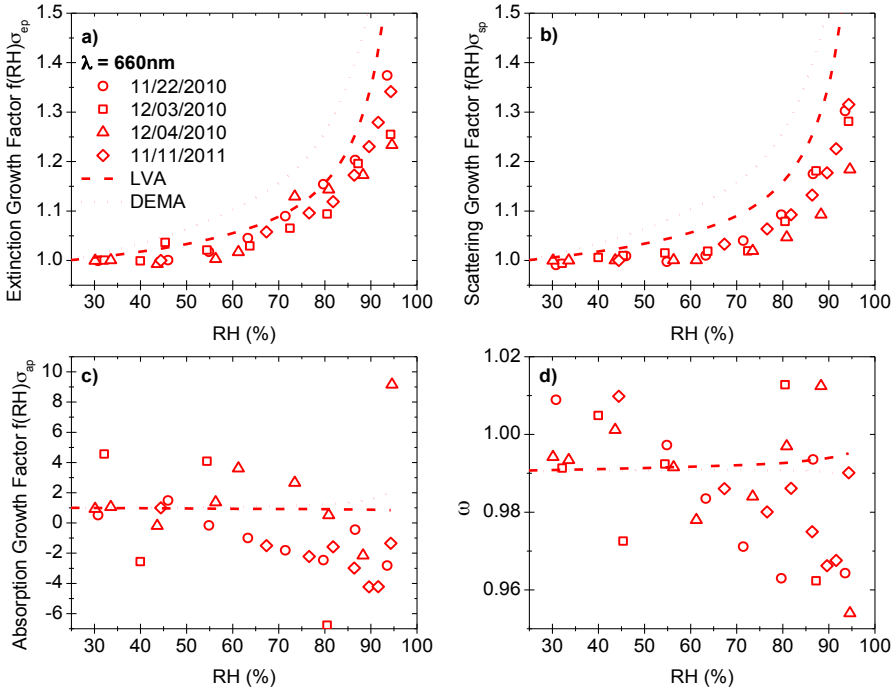

APPENDIX B

Filter analysis results for mixture experiments

Filter	Cl (ug)	NaCl (ug)	NaCl v	SO4 (ug)	NH42SO4 (ug)	NH42SO4 (v)	NO3 (ug)	Br (ug)	OC (ug)	POM	POM (v)	EC (ug)	Total Mass (ug)	Total Volume	%NaCl mass	%AS mass	%NaCl volume	%AS volume
BREM_N2010_6411	3.08	5.08	2.35	556.18	765.08	432.49	9.44	1.98	795.12	1335.80	1113.17	5.50	2122.87	1548.0	0.2	36.0	0.2	27.93873573
BREM_N2010_6412	15.18	25.02	11.56	306.70	421.90	238.49	5.97	1.74	617.84	1037.97	864.98	5.02	1497.62	1115.0	1.7	28.2	1.0	21.38901243
BREM_N2010_6413	21.28	35.08	16.20	152.97	210.43	118.95	0.52	0.31	334.37	561.73	468.11	5.85	813.92	603.3	4.3	25.9	2.7	19.71793175
BREM_N2010_6414	121.56	200.38	92.55	7.23	9.95	5.62	2.26	0.72	343.68	577.39	481.16	6.33	797.02	579.3	25.1	1.2	16.0	0.970452945
BREM_N2010_6415	137.64	226.88	104.80	7.17	9.86	5.58	1.49	0.40	280.73	471.62	393.02	9.68	719.94	503.4	31.5	1.4	20.8	1.10758498
BREM_N2010_6416	181.84	299.74	138.45	3.10	4.26	2.41	2.13	1.69	684.86	1150.56	958.80	6.21	1464.60	1099.7	20.5	0.3	12.6	0.219213115

APPENDIX C

OC/AS mixtures measured and modeled absolute optical data:

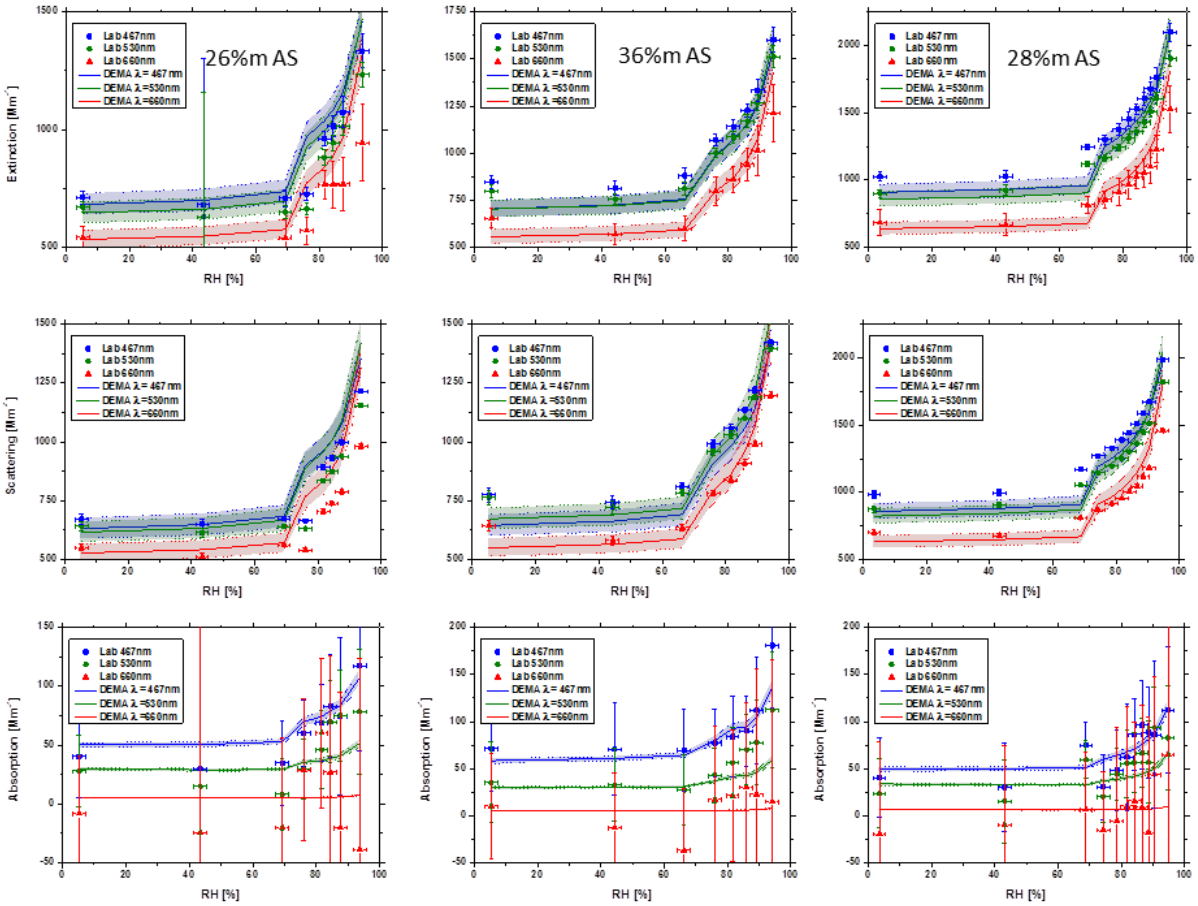

OC/NaCl mixtures measured and modeled absolute optical data: